Enhanced pressure drop, planar contraction flows and continuous spectrum models

M.F. Webster , H.R. Tamaddon-Jahromi , J.E. López-Aguilar , D.M. Binding

PII: S0377-0257(18)30325-2
DOI: https://doi.org/10.1016/j.jnnfm.2019.104184
Reference: JNNFM 104184

To appear in: *Journal of Non-Newtonian Fluid Mechanics*

Received date: 14 September 2018
Revised date: 7 October 2019
Accepted date: 8 October 2019

Please cite this article as: M.F. Webster , H.R. Tamaddon-Jahromi , J.E. López-Aguilar , D.M. Binding , Enhanced pressure drop, planar contraction flows and continuous spectrum models, *Journal of Non-Newtonian Fluid Mechanics* (2019), doi: https://doi.org/10.1016/j.jnnfm.2019.104184

Highlights

- A swAM model reflects enhanced pressure drops in planar contraction flows.
- A model with greater flexibility in control of first normal-stress difference response.
- Binding and Walters [1988] experimental pressure-drop data is quantitatively captured
- Transition states detected between flow phases of steady, oscillatory and unstable form
- Evolving patterns of salient-corner vortices and lip-vortex.

Enhanced pressure drop, planar contraction flows and continuous spectrum models*

M.F. Webster[a], H.R.Tamaddon-Jahromi[a1], J. E. López-Aguilar[a,b]
with
D.M. Binding[c]

[a]*Institute of Non-Newtonian Fluid Mechanics, Swansea University, College of Engineering, Bay Campus, Fabian Way, Swansea, SA1 8EN, UK*
[b]*Facultad de Química, Departamento de Ingeniería Química, Universidad Nacional Autónoma de México (UNAM), Ciudad Universitaria, Coyoacán, CDMX, 04510, Mexico*
[c]*Institute of Mathematics, Physics and Computer Science, University of Aberystwyth, Aberystwyth, SY23 3BZ, United Kingdom*

Abstract

This study addresses a rheological problem that has been outstanding now for the past few decades, raised by the experimental findings of Binding and Walters [1]. There, it was established experimentally that planar contraction flows for some Boger fluids could display enhanced pressure-drops above Newtonian flows, as was the case for their tubular counterparts. Nevertheless, flow-structures to achieve this result were reported to be markedly different, planar to circular. In this article, it is shown how predictive differential-viscoelastic solutions with continuum models can replicate these observations. Key to this success has been the derivation of a new definition for the third-invariant of the rate-of-deformation tensor in planar flows, mimicking that of the circular case [2-3]. This provides a mechanism to successfully incorporate dissipation within planar flows, as performed earlier for tubular flows. Still, to reach the necessary large deformation-rates to achieve planar enhanced pressure-drops, and whilst maintaining steady flow-conditions, it has been found crucial to invoke a continuous-spectrum relaxation-time model [3]. The rheological power and flexibility of such a model is clearly demonstrated, over its counterpart Maxwellian single-averaged relaxation-time approximation; the latter transcending the boundaries of steady-to-unsteady flow to manifest equivalent levels of enhanced pressure-drops. Then, the role of extensional viscosity and first normal-stress difference, each play their part to achieve such planar enhanced pressure-drops. As a by-product, the distinctive planar 'bulb-flow' structures discovered by Binding and Walters [1], absent in tubular flows, are also predicted under the associated regime of high deformation-rates where enhanced pressure-drop arise.

Keywords: Boger fluids; planar contraction flow; pressure-drop enhancement; *swAM* model

*Dedicated to the memory of our dear friend and colleague, late Professor Michael F. Webster

[1] Correspondence Author: *E-mail address*: cshamid@swansea.ac.uk

1. Introduction

Main theme and objective of this study may be outlined as follows. Having earlier quantitatively captured experimental vortex-trends and excess pressure-drops for Boger Fluids in *circular* contraction flows (López-Aguilar *et al.* [2, 3]), the focus shifts here to parallel this position for its counterpart of *planar* contraction flows, as demonstrated in Binding and Walters [1]. Such extraction of excess pressure-drops in circular flows by simulation was held as a significant breakthrough in differential-viscoelastic continuum-modelling (also paralleled by counterpart enhanced drag results for falling-sphere problem, see Garduño *et al.* [4, 5]). As such, one was already aware of the general trends observed in vortex-enhancement encountered for tubular flows with rise in flow-rate (Tamaddon-Jahromi *et al.* [6]), and the fact that this could also be replicated in planar sister flows, but only after some delay until higher deformation-rates had been reached (sharp-corner 4:1, López-Aguilar *et al.* [7]). The outstanding omission under predictive modelling, has been the distinct lack of progress made over the last thirty years or so, in capturing experimental pressure-drops for some Boger fluids in *planar* contraction configurations. The present analysis attempts to fill this void by meeting this deficiency.

Preliminary breakthroughs on numerical prediction of Boger fluids complex-flow experimental data

Firstly, it is informative to recognise the key advances found necessary to capture such tubular experimental excess pressure-drops (*epd*) for Boger fluids [7, 8]. That is prior to making the case for extending this success into the planar context. It was necessary to *enhance the relevant constitutive models* to imbue them with elements of dissipation, particularly responsive to extensional deformation, so that the constant shear-viscosity implied was not impaired. Then, it was found important to *replicate experimental protocols through predictive procedures*, to track steady viscoelastic solutions through rise in deformation-rate for fixed fluid-properties (as opposed to earlier common practice of adjusting fluid properties at fixed average deformation-rate). This lay in conjunction with various *advanced stabilization techniques* to pierce the setting of high deformation-rate steady viscoelastic solutions (retaining evolution tractability; akin to reaching *High Weissenberg number solutions* [9]). With these practical steps undertaken, the goal of extracting 4:1:4 tubular experimental excess pressure-drops for Boger fluids of Rothstein and McKinley [10] was realised with the *swIM* model, using an averaged Maxwelian relaxation-time. Predictive solutions in Tamaddon-Jahromi *et al.* [8], captured the initial pronounced rise in *epd* with flow-rate, large vortex-enhancement, the experimental limiting plateau for steady-solutions and the subsequent regime of unsteady oscillatory flow. Such *epd*-extraction was then further extended in López-Aguilar *et al.* [2] to the more extreme case of sharp-corner contraction flow, as reported by Nigen and Walters [11].

Further challenges on planar contraction flows Accordingly, one might have envisaged that findings for the counterpart planar configuration, would have followed naturally, and as a consequence of the above. Unfortunately, the distinction between circular and planar deformations reveals subtle differences that emerge in the representation of the flow-invariants, this being particularly apparent under extensional deformation with dependency on the *third-invariant* of the rate of deformation. Standard conventional treatment in the planar instance would provide a null result for the *third invariant*, whilst this has some non-vanishing and significant contribution to make under the circular setting. The consequence of this feeds into the functionality imposed on the dissipation boost, which was found necessary in circular flows to enhance pressure-drops above their Newtonian equivalents. Thus, following standard conventions and in planar flows, no such boost is provided, and there is no proof of any evidential excess pressure-drop. Hence, a new approach is required here for the planar context, in recognition of the separability and independence of each (*x*-*y*) plane from any other in the third *z*-dimension; the details are exposed below. In this manner, a new *in-plane* definition is extracted for planar extensional deformation, which follows the circular case by analogy. This provides the key to supplying the dissipation boost for the planar configuration, from which only then, the associated excess pressure-drops may be accessed.

Flow transitions at high flow-rates and their description Further pursuit of the relevant high flow-rate steady viscoelastic planar solutions, still retains some interesting aspects to address, and more particularly in respect of the steady-to-unsteady thresholds encountered under these more severe and dynamic flow states. It has been natural to first assess such solutions through an averaged Maxwellian single relaxation-time model approximation, using the *so-called swIM*–model [2]. Subsequently, one has appealed to the more general continuous-spectrum relaxation-time function *swAM*–approach [3]. The former discloses the difficulties faced in reaching the experimental pressure-drop data, with retention of steady solutions. Only pseudo-steady solutions could achieve this, principally through enhancement of the extensional viscosity properties. Under the more general continuous-spectrum function *swAM*–approximation of López-Aguilar et al. [3], further functional dependence on the first normal-stress difference is also introduced, which allows this model to additionally impact on the pressure-drop. In this manner, steady viscoelastic solutions are gathered at the bespoke flow-rates in question, and the recorded experimental data is recovered, including the kinematic flow-transitions described by Binding & Walters [1], with bulb-flow and instability prediction at medium-to-high flow-rates. Other computational work of relevance, addresses on pressure-drop and vortex-structures in a particular 8:1

abrupt tubular contraction flow of Tamaddon-Jahromi *et al.* [6] (see below versus Nigen and Walters [11]).

Further related work would include that of Oliveira *et al.* [12], where comprehensive numerical simulations were performed with a finite-volume method on two models, Oldroyd-B and linear Phan-Thien-Tanner (PTT). Such work addressed axisymmetric flow through abrupt contractions of varying contraction-ratio, from 2 up to 100. Usefully, these authors found the same extra pressure-drop (Couette correction) applied with rising Deborah number (*De*), for various contraction-ratios ranging from 10 to 100, and for Deborah number up to 100. There, the PTT extensibility parameter was also varied (ε=0 to 0.5) and found to impact on pressure-drop. For small values of ε, the Couette correction was a monotonically decreasing function of *De*, while for larger ε values, it became a monotonically increasing function of *De*.

Background studies Under citation of key comparative and background studies, for a detailed review of the many contributions to the study of contraction flows, the interested reader is referred to Tanner [13], Owens and Phillips [14], Walters and Webster [15], Aboubacar *et al.* [16, 17], Alves *et al.* [18], Phillips and Williams [19]. Experimentally, this covers both planar and circular configurations, the influence of contraction-ratio and rounding of sharp-corners (see, for example, Evans and Walters [20]; Boger *et al.* [21]; Binding and Walters [1]; Binding *et al.* [22]; Rothstein and McKinley [10, 23]; Nigen and Walters [11]). The case for Boger fluids and shear-thinning fluids was made in turn.

Relevant kinetic-theory models Under a molecular constitutive modelling approach, kinetic theory models provide a coarse-grained description of molecular configurations. Such models tackle important features that govern the flow-induced evolution of configurations. In recent years, kinetic theory has advanced well beyond the classical reptation tube-model by Doi & Edwards (see more details in Keunings [24]). An large number of Brownian dynamics studies have emerged based on Kramers chains, bead-spring chains and dumbbells, with macroscopic constitutive equations, namely the FENE–P, FENE–CR and FENE–L models, that are closely related to the FENE dumbbell kinetic theory. The interest in such theory has significantly advanced the understanding of polymer dynamics in general. Particularly, a comprehensive survey on mathematical formulation and numerical approaches, with a review of applications to polymer solutions and melts, liquid crystalline polymers and fibre suspension, is presented in Keunings [25]. Although kinetic theory models are much more demanding in terms of computer resources than conventional continuum computations, they allow the direct use of kinetic theory models in flow simulations, thus avoiding potentially inaccurate closure approximations (Ammar et al. [26, 27]). Furthermore, some constitutive equations applied in continuum modeling have

originated from molecular models and kinetic theory. This is typified through the pom-pom constitutive model introduced by McLeish & Larson [28], based on reptation dynamics of an idealized linear molecule with an equal number of branched arms at both ends (*see section 2.1 of this work and Refs. [2-8] on the main features of swIM and swAM models*).

Experimental studies on contraction flow of Boger fluids In the Boger fluid contraction flows of *Binding and Walters [1]*, of Fig.1 and Fig.2a, excess pressure losses were attributed to two distinct flow mechanisms. In the axisymmetric case, both vortex-enhancement and excess pressure loss were observed. In the planar case, there was substantial excess pressure loss at high flow-rates (but delayed over that of axisymmetric), yet without apparent vortex-enhancement, this being replaced instead with a *'bulb'* flow field in the vicinity of the re-entrant corner. In contrast, Nigen and Walters [11], as in Fig.2b, found significant differences in pressure-drop between Boger and Newtonian liquids in tubular flow. These authors attributed vortex-enhancement to a 'lip-vortex mechanism'; prior to encapsulating any salient-corner vortex, and subsequent vortex-growth, often to extravagant size (see Tamaddon-Jahromi *et al.* [6]). Interestingly, in Nigen and Walters [11] experiments, with their particular Boger fluid compositions (polyacrylamide PAA/glucose/water), no distinction could be drawn between corresponding pressure-drops for Newtonian and Boger fluids in planar configurations. So clearly, rheological distinction between different Boger fluids is a factor here. Notably, the *swIM*-predictions of Tamaddon-Jahromi *et al.* [6] for the Nigen and Walters [11] 8:1 tubular contraction flow, reflect well such experimental findings, under increasing flow-rate. There, rich vortex-characteristics were reflected, with significant vortex-enhancement captured, through evolving patterns of salient-corner, lip-vortex and elastic-corner vortices. As in the present study, rheological distinction could be drawn out over governing parameter-variation, through solvent-fraction (β), finite-extensibility parameter (L), and extensional-based dissipative time-scale parameter (λ_{D1}). In a similar vein, Rothstein and McKinley [10, 23] covered a large range of Deborah numbers for axisymmetric contraction-expansion flows, various contraction-ratios (between two and eight) and degrees of re-entrant corner curvature. There, large *epd* was observed for Boger fluids, above that for a Newtonian fluid, independent of contraction-ratio and re-entrant corner curvature.

Overview This study addresses the problem of matching experimental findings with numerical prediction for the extreme experimental levels of pressure-drops observed in contraction flows reported by Binding and Walters [1]. There, significant differences in response were observed between Boger and Newtonian fluids in steady-state *planar contraction* flow.

2. Governing equations, flow problem specification and numerical algorithm

For an incompressible fluid of density ρ, the equations of continuity and motion may be expressed as:

$$\begin{aligned} &\nabla\cdot\boldsymbol{u}=0,\\ &\rho\frac{\partial\boldsymbol{u}}{\partial t}=\nabla\cdot\boldsymbol{T}-\rho\,\boldsymbol{u}\cdot\nabla\boldsymbol{u}-\nabla p,\\ &\boldsymbol{T}=\boldsymbol{\tau}_{\mathrm{p}}+2\eta_s\boldsymbol{D}, \end{aligned} \tag{1}$$

with velocity vector $\boldsymbol{u}$, fluid density ρ, total stress $\boldsymbol{T}$, time t, rate-of-deformation tensor $\boldsymbol{D}=\left(\nabla\boldsymbol{u}+\nabla\boldsymbol{u}^{\dagger}\right)/2$, and solvent viscosity η_s. The total stress $\boldsymbol{T}$ is decomposed into two parts, a viscous component ($2\eta_s\boldsymbol{D}$) and a polymeric component ($\boldsymbol{\tau}_p$). An equation-of-state for the polymeric stress completes the system of equations.

2.1. Discrete-Spectrum (*swIM*) and Continuous-Spectrum (*swAM*) approximations

2.1.1 Rheology of the swIM model – discrete-spectrum approximation, single-mode

The (*swIM*) constitutive equation may be expressed through the total-stress, $\boldsymbol{T}$, the configuration-tensor, $\boldsymbol{A}$, and the deformation-rate tensor, $\boldsymbol{D}$, as:

$$\boldsymbol{T}=\frac{\eta_p}{\lambda_1}\,f\left(\mathrm{Tr}(|\boldsymbol{A}|)\right)(\boldsymbol{A}-\mathbf{I})\phi(\dot{\varepsilon})+2\eta_s\phi(\dot{\varepsilon})\boldsymbol{D}. \tag{2}$$

This is Kramers rule, where the dissipative-function $\phi(\dot{\varepsilon})$ is defined as $\phi(\dot{\varepsilon})=1+\left(\lambda_{D1}\dot{\varepsilon}\right)^2$, based on a dissipative material time-scale parameter of (λ_{D1}), and a generalised strain-rate invariant $(\dot{\varepsilon})$. Here λ_1 is a relaxation-time, η_{p} is a polymeric viscosity, and $\eta_0=\eta_{\mathrm{s}}+\eta_{\mathrm{p}}$ is a zero shear-rate viscosity, as $(\dot{\gamma}\to 0)$. Under Boger-fluid approximation with constant functions $\{\eta_{\mathrm{s}},\eta_{\mathrm{p}}\}$, the corresponding solvent-fraction ratio is $\beta=\eta_{\mathrm{s}}/\left(\eta_{\mathrm{s}}+\eta_{\mathrm{p}}\right)$, so that equivalently $\{\eta_{\mathrm{s}}=\beta\eta_0,\eta_{\mathrm{p}}=(1-\beta)\eta_0\}$.

Then, the equation for configuration-tensor $\boldsymbol{A}$, is that taken from the base FENE-CR model, as:

$$\lambda_1\overset{\nabla}{\boldsymbol{A}}+f\left(Tr(|\boldsymbol{A}|)\right)(\boldsymbol{A}-\mathbf{I})=0, \tag{3}$$

where the upper-convected material-derivative of the configuration-tensor is ($\overset{\nabla}{\boldsymbol{A}}$), defined as:

$$\overset{\nabla}{\boldsymbol{A}}=\frac{\partial\boldsymbol{A}}{\partial t}+\mathbf{u}\cdot\nabla\boldsymbol{A}-(\nabla\mathbf{u})^{\dagger}\cdot\boldsymbol{A}-\boldsymbol{A}\cdot(\nabla\mathbf{u}), \tag{4}$$

and the corresponding fluid internal-structure functional, $f\left[Tr(|\boldsymbol{A}|)\right]$, is defined on the trace $(|\boldsymbol{A}|)$ and the Hookean-dumbell bead-chain length L (an extensibility-parameter):

$$f(Tr(|\boldsymbol{A}|)) = \frac{1}{1 - Tr(|\boldsymbol{A}|)/L^2}. \quad (5)$$

Non-dimensional Weissenberg number may be defined as $Wi = \lambda_1 \frac{U_{avg}}{\ell}$, which, through non-dimensionalisation, appears in Eq.(3) modulating the viscoelastic response of the material. Here, U_{avg} is an averaged characteristic-velocity, based on the flow-rate (Q), and ℓ is a characteristic length. The latter may be taken as the radius of constriction (circular), or half constriction gap-width (planar). Note that, since $Q/Area = U_{avg}$ and $Wi = U_{avg} * (\lambda_1 / \ell)$, then the Weissenberg number may be redefined as $Wi = (Q/Area) * (\lambda_1 / \ell)$. Consequently, $(Q/Q_0)^{Sim} = (Wi/Wi_0)^{Sim}$. Therefore, by employing $(Q/Q_0)^{Sim}$ instead of $(Wi/Wi_0)^{Sim}$, one may have a direct comparison between pressure-drop and vortex-intensity. In this study, numerical predictions for the planar case, where compared with the planar experimental-data of Binding and Walters [1], are in terms of a relative flow-rate (Q/Q_0) measure of $(Q/Q_0)^{Exp} = (Q/Q_0)^{Sim}$, and $\Delta P_0^{Sim} = 550$ pressure units, whilst selecting $\ell = 1$ unit and $\lambda_1^{Sim} = 1$ sec. The relative flow-rate (Q/Q_0) for the circular case is taken to be $(Q/Q_0)^{Exp} = (Q/Q_0)^{Sim}$; see appendix for more details on scaling and boundary conditions for the planar and circular configurations.

The associated rheometrical functions for the *swIM* model, of shear viscosity η_{Shear}, first normal-stress difference in shear N_1^{Shear} and planar extensional viscosity η_E can be represented accordingly, as:

$$\eta_{Shear} = \eta_0,$$
$$N_{1Shear} = \frac{2\eta_p \lambda_1 \dot{\gamma}^2}{f}, \quad (6)$$
$$\eta_E = 4\phi(\dot{\varepsilon})\left[\eta_s + \eta_p \left\{\frac{f^2}{(f - 2\lambda_1\dot{\varepsilon})(f + 2\lambda_1\dot{\varepsilon})}\right\}\right].$$

Discussion on the two key rheological functions for the *swIM* model, of first normal-stress difference and planar extensional viscosity, is furnished through Fig.3, where one can distinguish departure from Oldroyd-B and base FENE-CR functionality, under a fixed-reference solvent-fraction of (β=0.9). There, variation in extensibility factor is ($5 \le L \le 12$) and on dissipation factor is ($0 \le \lambda_{D1} \le 0.6$). With *swIM*-response, the first normal-stress difference response (N_1^{Shear}) follows that of FENE-CR; this implies that there is weakening of N_1^{Shear} at mid-range deformation-rates as L-declines (Fig.3b). Likewise, one also expects some N_1^{Shear}-weakening with rise in solvent-fraction from β=0.9 to 0.95. On extensional viscosity (Fig.3a), there is a rising trend in *swIM*-response with $\lambda_{D1} > 0$, when compared

against that for FENE-CR(λ_{D1}=0); in addition, extensional viscosity rises sharply around $\lambda_1\dot{\gamma}$=5*10^{-1} units.

2.1.2 Rheology of the swAM model – continuous-spectrum function approximation

The starting point in motivation and derivation for the continuous-spectrum function approximation embodied in the *swAM model* lies in the detail presented in López-Aguilar *et al.* [3]. As such, this follows as a functional generalization of the precursor *swIM model*, via a White–Metzner construction with both viscous and polymeric contributions, matching the functional form derived for viscous response [$\eta(\dot{\gamma},\dot{\varepsilon})$] to a counterpart form on elastic material-time response [$\lambda(\dot{\gamma},\dot{\varepsilon})$]; embodying *two master functions*. Whilst retaining sufficient generality, this representation assumes *functional separability* across shear and extensional deformation. Crucially, this *swAM model* offers additional rheological control across wider rate ranges above and beyond the capability of the sister *swIM model*, which in particular has greatest impact upon control of N_1-variation. Though implemented in conformation-tensor (***A***)-form, the model can be expressed in equivalent ($\boldsymbol{\tau}_s,\boldsymbol{\tau}_p$)-form, through {$\eta_s,\eta_p$}-splits as:

$$\begin{aligned}&\boldsymbol{\tau}_s = 2(\eta_s)\phi(\lambda_{D1}\dot{\varepsilon})\boldsymbol{D},\\ &f\boldsymbol{\tau}_p + \alpha\lambda_1 * \lambda(\dot{\gamma},\dot{\varepsilon})\overset{\nabla}{\tau}_p = 2\eta_p\eta(\dot{\gamma},\dot{\varepsilon})f\boldsymbol{D},\end{aligned} \tag{7}$$

where one may identify the *two master functions*, {$\lambda(\dot{\gamma},\dot{\varepsilon}),\eta(\dot{\gamma},\dot{\varepsilon})$}, and their respective sub-functions, $\lambda(\dot{\gamma},\dot{\varepsilon})\to\lambda_{sh}(\lambda_1\dot{\gamma})\lambda_{ext}(\lambda_{D2}\dot{\varepsilon})$, and $\eta(\dot{\gamma},\dot{\varepsilon})\to\eta_{sh}(\lambda_1\dot{\gamma})\eta_{ext}(\lambda_{D1}\dot{\varepsilon})$, alongside their constant base-reference factors {λ_1 , η_0}. The outcome is a requirement for *four* sub-functions: {$\lambda_{sh}(\lambda_1\dot{\gamma}),\lambda_{ext}(\lambda_{D2}\dot{\varepsilon}),\eta_{sh}(\lambda_1\dot{\gamma}),\eta_{ext}(\lambda_{D1}\dot{\varepsilon})$}, such that:

$$\begin{aligned}&\lambda(\dot{\gamma},\dot{\varepsilon}) = \lambda_1 * \lambda_{sh}(\lambda_1\dot{\gamma})\lambda_{ext}(\lambda_{D2}\dot{\varepsilon}),\quad \lambda_{ext}(\dot{\varepsilon}\to 0)=1,\\ &\eta(\dot{\gamma},\dot{\varepsilon}) = \eta_0 * \eta_{sh}(\lambda_1\dot{\gamma})\eta_{ext}(\lambda_{D1}\dot{\varepsilon}),\quad \eta_{ext}(\dot{\varepsilon}\to 0)=1,\quad \eta_{sh}(\dot{\gamma}\to 0)=1.\end{aligned} \tag{8}$$

In the present fluid-material context of interest, that of Boger Fluids, one can take $\eta_{sh}(\lambda_1\dot{\gamma})=1\ \ \forall\,\dot{\gamma}\geq 0$, which leaves a specification requirement for *three* sub-functions: {$\lambda_{sh}(\lambda_1\dot{\gamma})$, $\lambda_{ext}(\lambda_{D2}\dot{\varepsilon}),\eta_{ext}(\lambda_{D1}\dot{\varepsilon})$}. From the *swIM*-derivation, one can extract:

$$\eta_{ext}(\lambda_{D1}\dot{\varepsilon}) = \phi(\lambda_{D1}\dot{\varepsilon}) = 1+\left(\lambda_{D1}\dot{\varepsilon}\right)^2, \tag{9}$$

leaving the remaining *two* sub-functions on elastic material-time response to specify. These were suggested in [3], as:

$$\lambda_{sh}(\lambda_1\dot{\gamma}) = \frac{1}{\left[1+(\lambda_1\dot{\gamma})^2\right]^{m_1}},\ \lambda_{ext}(\lambda_{D2}\dot{\varepsilon}) = \frac{1}{\left[1+(\lambda_{D2}\dot{\varepsilon})^2\right]^{m_2}}. \tag{10}$$

This leads one to the realisation that the shear sub-functions $\{\lambda_{sh}(\varphi), \eta_{sh}(\varphi)\}$, of the continuous spectrum (*swAM*)-model, allow one to predict exactly, the *shear viscosity* (η_{shear}) *and first normal stress difference* (N_1^{Shear}) in steady simple shear flows, whilst $\varphi \geq 0$ (being φ a relevant shear-rate); and simultaneously, whilst $\varphi \leq 0$, these *same two functions but in a shifted range*, can match the dynamic oscillatory shear-data of dynamic viscosity ($\eta'(\omega)$) and storage modulus ($G'(\omega)$), where ω represents the frequency in the oscillatory test. Independently, extensional viscous-response can be predicted exactly through the two sub-functions $\{\lambda_{ext}(\lambda_{D2}\dot{\varepsilon}), \eta_{ext}(\lambda_{D1}\dot{\varepsilon})\}$ (Binding [32], López-Aguilar *et al.* [3]). Hence, in practical terms, and as necessity dictates, the (*swAM*)-model, with *two* constant base-reference factors $\{\lambda_1, \eta_0\}$, *two* additional time-constants $\{\lambda_{D1}, \lambda_{D2}\}$ and *two* power-indices $\{m_1, m_2\}$, can be manipulated to provide any common extensional viscosity response. Independent weighting of purely-dissipative and mixed dissipative stress contributions is ensured. In addition, the power-indices $\{m_1, m_2\}$ may be identified by matching to the experimental data for any particular polymeric liquid. Thus, $\{m_1\}$ may be generated from shear-viscosity (η_{Shear}) and first normal-stress difference (N_1^{Shear}) data; and $\{m_2\}$ likewise, from extensional viscosity data.

As above for the *swAM* model, one may extract the corresponding functional-forms for the key rheological properties of interest, the planar extensional-viscosity and first normal-stress difference, viz.:

$$\eta_E = 4\phi(\dot{\varepsilon})\left[\eta_s + \eta_p\left\{\frac{f^2}{[f-2\alpha\lambda_1\lambda_{sh}(\lambda_1\dot{\varepsilon})\lambda_{ext}(\lambda_{D2}\dot{\varepsilon})\dot{\varepsilon}][f+2\alpha\lambda_1\lambda_{sh}(\lambda_1\dot{\varepsilon})\lambda_{ext}(\lambda_{D2}\dot{\varepsilon})\dot{\varepsilon}]}\right\}\right],$$
$$\lambda_{sh}(\lambda_1\dot{\varepsilon}) = \frac{1}{\left[1+3(\lambda_1\dot{\varepsilon})^2\right]^{m_1}}, \tag{11}$$
$$N_1^{Shear} = \frac{2\eta_p\alpha[\lambda_{sh}(\lambda_1\dot{\gamma})]\dot{\gamma}^2}{f} = \frac{2\eta_p\alpha\lambda_1\dot{\gamma}^2}{f\left[1+(\lambda_1\dot{\gamma})^2\right]^{m_1}}.$$

Such functional variation is charted in Fig.4, whereby one may differentiate variation in each function with alternative parameter setting, and draw distinction between *swIM* and *swAM* response. So, for example, considering extensional viscosity (Fig.4a), *swAM*-η_E (m_1=0.1) underestimates *swIM*-η_E at rates $0.4 < \lambda_1\dot{\varepsilon} < 10$; whilst, *swAM*($m_1$=-0.1) overestimates *swIM*-η_E at rates $0.4 < \lambda_1\dot{\varepsilon} < 15$. Alternatively in Fig.4b, on first normal-stress difference and contrasting against *swIM*, N_1^{shear} of *swAM*(m_1=0.1) proves uniformly weaker, whilst it is consistently stronger with *swAM*(m_1=-0.1, -0.25). On this basis, one may

proceed below to draw out rheological reasoning for the trends in pressure-drop observed. In addition, in Fig.4c, distinction in extensional-viscosity (η_E) is established between *swAM*(m_1=-0.1, m_2=zero) and *swAM*(m_1=-0.1, m_2=non-zero) models, through adjustment of the m_2-power-index. Here, *swAM* (m_1=-0.1, m_2=0.2) represents an underestimate of *swAM*(m_1=-0.1, m_2=zero) at rates $1.0 < \lambda_1\dot{\varepsilon} < 10$, whilst *swAM*($m_1$=-0.1, m_2=-0.2) provides an overestimate at rates $1.0 < \lambda_1\dot{\varepsilon} < 20$. Notably, both *swAM*($m_1$=-0.1, m_2=0.2) and *swAM*(m_1=-0.1, m_2=-0.2) share the same first normal-stress difference (N_1^{Shear}) with *swAM*(m_1=-0.1, m_2=zero) model (Fig.4c).

Overall, these two novel *swIM* and *swAM* models represent well the rheology of the Boger fluids considered in the present work as target experimental model-fluids, as it is apparent in Fig.3-5. These fluids are based on diluted constant shear-viscosity highly-elastic Boger solutions under two compositions, i.e. a maltose-syrup/water/polyacrylamide solution used in Binding & Walters [1] (1988), and a corn-syrup/water/polyacrylamide solution reported in Nigen & Walters [11] (2002). These fluids, particularly those reported in Binding & Walters [1] (1988), display a nearly constant shear-viscosity, with a steep quadratic N_{1Shear}-rise that softens with shear-rate increase, with an extensional viscosity η_{Ext}-response in a steep rising-trend with extension-rate.

In terms of the thermodynamic consistency of this swanINNFM(Q) model-family (*swIM* and *swAM* models) [2-3, 7-8], their origin trace back to the robust developments of Chilcott and Rallison [29] through their Finite Extendible Nonlinear Elasticity FENE-CR model-variant and its networked structure-function, whilst supplemented with a novel extra extensional-dissipation component of White-Metzner-type (White and Metzner [30]). These family of fluids enjoys the benefits of further generalised corrections and numerical implementations to ensure their thermodynamically consistent, in the form of the ABS-*f* correction (López-Aguilar el at. [9, 31]). Particularly, the ABS-*f* correction acts upon the fluid-structure *f*-functional, to enact proper physical-property estimation (such as viscosity) and to comply with the 2nd Law of Thermodynamics. This correction is of general nature, and is implemented through the absolute-value of the driving flow-invariant in the internal-structure *f*-functional (López-Aguilar el at. [9, 31]); in the case of the *swIM* and *swAM* family of fluids, the ABS-*f* correction appears on the trace of conformation-tensor $\boldsymbol{A}$ in Eq. (5).

2.2 Flow problem specification

In this study, the flow problem is that of creeping flow within a 4:1 planar contraction. The geometry is one that possesses sharp-corners, to reflect re-entrant corner behaviour and mimic the

experimental set-up. Extensive mesh-refinement has been performed in previous articles (Tamaddon-Jahromi *et al*. [6], Webster *et al.* [33]), satisfactorily establishing accuracy and mesh-convergence. As a consequence of these studies and to suit present purposes, here a medium mesh with 2897 quadratic-elements, 6220 nodes, and 32717 degrees-of-freedom (*dof*) is retained, see [33] for more details on 4:1 meshes.

To assess the time-stepping convergence, a temporal relative-increment L_2-norm is defined per variable. This, then, governs convergence of the time-stepping process, and is interpreted against a set tolerance-threshold (*Tol*), viz., $\mathrm{E}^{\mathrm{T}}(\mathrm{X}) = \dfrac{\| \mathrm{X}^{\mathrm{n+1}} - \mathrm{X}^{\mathrm{n}} \|}{1 + \| \mathrm{X}^{\mathrm{n+1}} \|} \leq \mathrm{Tol}$. The tolerance-threshold for acceptance of steady-state solution is typically set at 10^{-6}. A typical time-step size is of order $\mathrm{O}(10^{-4})$.

On boundary conditions, no-slip is applied on solid boundaries, with shear-free symmetry on the flow centreline [9]. Velocity and stress are imposed at flow-inlet, in keeping with full-developed steady-state flow and with vanishing inflow convection conditions. This only leaves a pressure-level to set at outlet. Steady-state solution continuation is adopted, through chosen initial-conditions, via prior flow-rate or alternative parameter solution, as befitting each situation encountered. In principal, a flow-rate-increase mode is favoured, as opposed to an increase in fluid elasticity, as described elsewhere (López-Aguilar et al. [2]; Tamaddon-Jahromi *et al.* [8]).

The pressure-drop (Δp) and flow-rate (Q) are scaled, respectively, using base-values extracted from the experimental studies of Binding and Walters [1] of $\Delta p_0^{\mathrm{Exp}} = 10^4$ Pa and $Q_0^{\mathrm{Exp}} = Q_0 \left[10^{-6} (\mathrm{m}^3 / \mathrm{s}) \right]$; see Fig.1 & 2b. This provides for scaling of the corresponding Newtonian flows (of comparable viscosities), establishing unity in $(Q/Q_0)^{\mathrm{Exp}}$, and parity at low deformation-rates between Boger fluid and Newtonian pressure-drop data. This is performed independently on circular and planar data, so that, in each case, pressure-drops can be interpreted on their own difference from their equivalent Newtonian fluid.

2.3 Numerical algorithm - a subcell finite element/finite volume scheme

The numerical algorithm employed is a well-founded hybrid scheme of finite-element (*fe*) and finite-volume (*fv*) form, being both second-order accurate and consistent in time, see (Wapperom and Webster [34]; Aboubacar and Webster [16]; Webster *et al*. [35]). It is a time-stepping, fractional-staged (three) equation formulation. The constitutive stress-equation is resolved via a subcell/cell-vertex finite-volume (*fv*) scheme; whilst the momentum-continuity equation subset is handled through a combination of incremental pressure-correction and a Taylor-Petrov-Galerkin (*fe*) schemes, applied over a parent-cell

triangular tesselation. This choice meets the respective typing of these equations with their various space-time properties. On the parent *fe*-grid, velocity-pressure interpolation is quadratic-linear, respectively. With four *fv*-subcells per parent *fe*-triangular-cell, each subtended *fv*-sub-cell is constructed by connecting the mid-side nodes of the parent *fe*-cells. Stress variables are located at *fv*-sub-cell vertices, avoiding solution reprojection, and yielding equivalent to linear stress-interpolation per child subcell. The temporal stress-equation has conservation-form, which is non-linear and has inhomogeneous source terms. On time-convection terms, fluctuation-distribution for fluxes (upwinding) is the scheme of choice, alongside a median-dual-cell treatment for source terms. Then on each time-step, a mixture of direct and iterative solvers is employed, leading to a highly effective and space-efficient implementation, well-oriented to parallelisation.

More recently, a series of improved stabilization techniques have been developed to handle viscoelastic solution tractability, and more generally, solution acquisition under severe flow conditions. These now lie well-documented in López-Aguilar *et al.* [2, 9]. This series would include - use of velocity-gradient recovery, a uniform discrete continuity correction, and additional compatibility conditions satisfied on the pure-extension flow-centreline; the imposition of absolute value on structure-network function (*f*) in the constitutive equation (*f-ABS*) and within Kramers' transformation; use of configuration variables in the stress-equation; continuation through steady-state solutions via flow-rate (*Q*)-rise, as opposed to elasticity-increase; and use of feedforward exit-procedures on velocity-gradients.

3. Flow invariants and alternative measures in circular and planar deformations

I - Circular: conventional shear and extensional flow-invariants and regularisation

First, with coordinates $(x_1, x_2, x_3)=(z, r, \theta)$, one considers the rate-of-strain tensor $\boldsymbol{D}$, with its *in-plane* D_{rz}-subtensor indicated in the red-dashed square:

$$\boldsymbol{D} = \begin{bmatrix} \dfrac{\partial u_z}{\partial z} & \dot{\gamma} & 0 \\ \dot{\gamma} & \dfrac{\partial u_r}{\partial r} & 0 \\ 0 & 0 & \dfrac{\partial u_\theta}{\partial \theta} \end{bmatrix} , \qquad (12)$$

where, under steady simple-shear flow and generalised coordinates (in which one may take the axial velocity-component u_z as the flow-direction velocity u_1, the radial velocity-component u_r as the velocity-component in the gradient-direction u_2, and the azimuthal velocity component u_θ as the velocity-component in the neutral direction u_3), one may identify velocity and stress functional-forms as:

$$\begin{aligned} &u_1 = \dot{\gamma} x_2, \quad u_2 = u_3 = 0, \\ &\sigma_{12} = \sigma = \dot{\gamma}\eta(\dot{\gamma}), \\ &\sigma_{11} - \sigma_{22} = N_1(\dot{\gamma}), \\ &\sigma_{22} - \sigma_{33} = N_2(\dot{\gamma}). \end{aligned} \tag{13}$$

Similarly, under uniaxial extensional flow, one gathers:

$$\begin{aligned} &u_1 = \dot{\varepsilon} x_1, \quad u_2 = -\frac{\dot{\varepsilon} x_2}{2}, \quad u_3 = -\frac{\dot{\varepsilon} x_3}{2}, \\ &\sigma_{11} - \sigma_{22} = \sigma_{22} - \sigma_{33} = \dot{\varepsilon}\eta_E(\dot{\varepsilon}), \end{aligned} \tag{14}$$

for which:

$$\boldsymbol{D} = \begin{bmatrix} \dot{\varepsilon} & 0 & 0 \\ 0 & -\dot{\varepsilon}/2 & 0 \\ 0 & 0 & -\dot{\varepsilon}/2 \end{bmatrix} . \tag{15}$$

As a consequence, one may identify the various derived invariants and functions:

$$\det(\boldsymbol{D}_{rz}) = \frac{\partial u_r}{\partial r}\frac{\partial u_z}{\partial z} - \dot{\gamma}^2; \ \dot{\gamma} = \frac{1}{2}\left(\frac{\partial u_r}{\partial z} + \frac{\partial u_z}{\partial r}\right); \qquad trace(\boldsymbol{D}) = \left(\frac{u_r}{r}\right) + \left(\frac{\partial u_r}{\partial r} + \frac{\partial u_z}{\partial z}\right) = 0. \tag{16}$$

Then, the second-invariant of $\boldsymbol{D}$, is:

$$I_2^{axi} = \frac{1}{2}\det(\boldsymbol{D}^2) = \frac{1}{2}\left[\left(\frac{\partial u_r}{\partial r}\right)^2 + \left(\frac{\partial u_z}{\partial z}\right)^2 + \left(\frac{u_r}{r}\right)^2 + \frac{1}{2}\left(\frac{\partial u_r}{\partial z} + \frac{\partial u_z}{\partial r}\right)^2\right], \tag{17}$$

and, the third-invariant of $\boldsymbol{D}$,

$$I_3^{axi} = \det(\boldsymbol{D}) = \left(\frac{u_r}{r}\right)\left[\frac{\partial u_r}{\partial r}\frac{\partial u_z}{\partial z} - \frac{1}{4}\left(\frac{\partial u_r}{\partial z} + \frac{\partial u_z}{\partial r}\right)^2\right] = \left(\frac{u_r}{r}\right)\left[det(\boldsymbol{D}_{rz})\right]. \tag{18}$$

One recognizes in the circular context, in I_3^{axi} (Eq.18), the product dependency upon $\det(\boldsymbol{D}_{rz})$ and the *out-of-plane* extensional component $\left(\frac{u_r}{r}\right)$. Yet, from continuity and via the identity $trace(\boldsymbol{D}) = 0$, the *out-of-plane* extensional component $\left(\frac{u_r}{r}\right)$ can be directly related to the *in-plane* extensional components, viz.:

$$\left(\frac{u_r}{r}\right) = -\left(\frac{\partial u_r}{\partial r} + \frac{\partial u_z}{\partial z}\right) = \text{- trace } (\boldsymbol{D}_{rz}).$$

Hence, one may rewrite I_3^{axi} in terms of its equivalently *in-plane* interpretation, with segregation of shear and extensional components, as:

$$I_3^{axi} = \det(\boldsymbol{D}) = -\left(\frac{\partial u_r}{\partial r} + \frac{\partial u_z}{\partial z}\right)\left[\det(\boldsymbol{D}_{rz})\right] = -trace(\boldsymbol{D}_{rz})\det(\boldsymbol{D}_{rz}). \tag{19}$$

One notes, beyond the ideal deformation settings above, and whilst maintaining frame-invariance, a generalised shear-rate ($\dot{\gamma} = \Gamma_{gen}^{axi}$) and extension-rate ($\dot{\varepsilon} = \Sigma_{gen}^{axi}$) may be defined on the basis of the second invariant (I_2) and third invariant (I_3) of $\boldsymbol{D}$ (see Debbaut and Crochet [36]), yielding:

$$\Gamma_{gen}^{axi} = 2\sqrt{I_2}\,, \qquad \Sigma_{gen}^{axi} = 3I_3^{axi} / (\delta_{\text{reg}} + I_2^{axi}). \tag{20}$$

In the above, constant components satisfy suitable specification in pure shear and extension, and regularization is imposed through the δ_{reg}–factor [small, typically ~O(10^{-4})], on the denominator of Σ_{gen}^{axi}, to ensure a generalized and robust definition for extension. This guards against the situation where I_2 may tend to zero, as would occur for example on the symmetry centreline in shear-free flow. From Debbaut and Crochet [36], instead, one may look at the alternative choice of $\dot{\varepsilon} = \sqrt[3]{4III_d}$, to avoid reference to the second-invariant and regularization. Yet still, this form is found lacking in inhomogeneous complex flow with both shear and extension arising, wherever sharp gradients on the deformation are present (as here with a flow singularity). This exposes the issue of solution tractability, and the need for scaling of the third-invariant with the second-invariant, revealing its nature in the wider flow context. Further alternative definitions that have been explored (but discarded) are provided in Table 5, where their deficiencies are also identified; crucially, the lack of a shear contribution to the third-invariant, in inhomogeneous complex flow.

II - Planar: conventional shear and extensional flow-invariants and regularization

Mirroring the circular configuration theory above, one may now pass to consider the planar equivalent rate-of-strain tensor $\boldsymbol{D}$, with coordinates $(x_1, x_2, x_3)=(x, y, z)$ and its *in-plane* $\boldsymbol{D}_{xy}$-subtensor (boxed in dashed red), as indicated:

$$\boldsymbol{D}=\begin{bmatrix} \dfrac{\partial u_x}{\partial x} & \dot{\gamma} & 0 \\ \dot{\gamma} & \dfrac{\partial u_y}{\partial y} & 0 \\ 0 & 0 & 0 \end{bmatrix} . \tag{21}$$

Now, under steady simple-shear deformation and generalised coordinates (and accordingly, relating u_x to u_1, u_y to u_2 and u_z with u_3), again one may identify velocity and stress functional-forms as:

$$\begin{aligned} &u_1=\dot{\gamma}x_2, \quad u_2=0, \quad u_3=0, \\ &\sigma_{12}=\sigma=\dot{\gamma}\eta(\dot{\gamma}), \\ &\sigma_{11}-\sigma_{22}=N_1(\dot{\gamma}), \end{aligned} \tag{22}$$

whilst, under planar extensional flow, one gathers:

$$\begin{aligned} &u_1=\dot{\varepsilon}x_1, \quad u_2=-\dot{\varepsilon}x_2, \quad u_3=0, \\ &\sigma_{11}-\sigma_{22}=\dot{\varepsilon}\eta_E(\dot{\varepsilon}), \end{aligned} \tag{23}$$

whence,

$$\boldsymbol{D}=\begin{bmatrix} \dot{\varepsilon} & 0 & 0 \\ 0 & -\dot{\varepsilon} & 0 \\ 0 & 0 & 0 \end{bmatrix}. \tag{24}$$

This leads to counterpart, derived invariants and functions:

$$\det(\boldsymbol{D}_{xy})=\frac{\partial u_x}{\partial x}\frac{\partial u_y}{\partial y}-\dot{\gamma}^2; \qquad \dot{\gamma}=\frac{1}{2}\left(\frac{\partial u_x}{\partial y}+\frac{\partial u_y}{\partial x}\right); \qquad trace(\boldsymbol{D})=\left(\frac{\partial u_x}{\partial x}+\frac{\partial u_y}{\partial y}\right)=0, \tag{25}$$

where, the second-invariant of $\boldsymbol{D}$, is:

$$I_2^{plane} = \frac{1}{2}\det(\boldsymbol{D}^2) = \frac{1}{2}\left[\left(\frac{\partial u_x}{\partial x}\right)^2 + \left(\frac{\partial u_y}{\partial y}\right)^2 + \frac{1}{2}\left(\frac{\partial u_x}{\partial y} + \frac{\partial u_y}{\partial x}\right)^2\right]. \quad (26)$$

Following the logics above from the circular setting, in the planar case, the third-invariant ($I_3^{plane-abs}$) can also be expressed in terms of *in-plane* components alone. However, one observes now, the necessity of taking absolute values within the trace function, as in $trace(|\boldsymbol{D}_{xy}|)$, to ensure a non-zero quantification of *in-plane* extension (as secured in the circular case). Standard convention would otherwise return a null value, since $(trace(\boldsymbol{D}_{xy}) = 0)$ from continuity. This identifies the key-distinction between these two alternative forms of deformation, in planar extension and uniaxial extension. Under planar extension, each (*xy*)-plane *(in-plane)* contribution is uncoupled, and therefore, independent of the third (*z*)-dimension *(out-of-plane)* contribution. In the circular case, this is not the case, where *in-plane* and *out-of-plane* components are linked. Thus:

$$I_3^{plane-abs} = \det(\boldsymbol{D}) = -\left(\left|\frac{\partial u_x}{\partial x}\right| + \left|\frac{\partial u_y}{\partial y}\right|\right)\left[\det(\boldsymbol{D}_{xy})\right] = -trace(|\boldsymbol{D}_{xy}|)\det(\boldsymbol{D}_{xy}). \quad (27)$$

Beyond ideal deformation, this yields equivalent generalised shear-rate ($\dot{\gamma} = \Gamma_{gen}^{plane} = 2\sqrt{I_2}$) and extension-rate ($\dot{\varepsilon} = \Sigma_{gen}^{plane-abs}$), with suitable constants and regularization, where now accordingly,

$$\Sigma_{gen}^{plane-abs} = -(0.5 * I_3^{plane-abs}) / (\delta_{reg} + I_2^{plane}). \quad (28)$$

Field distributions of these quantities, in the circular and planar context, are displayed under the results section below, where one can compare directly the quantification of extension extracted under each deformation setting. This may be mirrored in the counterpart, all-important dissipation contributions generated under $\phi(\dot{\varepsilon}) = 1 + (\lambda_{D1}\dot{\varepsilon})^2$, noted as an even function of extension-rate, see below for more detail.

4. Planar versus circular comparison, streamlines and third-invariant definition – *swIM predictions*

In this section, evidence is provided of the benefits rendered from the proposed third-invariant definition $I_3^{plane-abs}$ and its consequences in the estimation of the extension rate in complex flow. Solution flow

fields are reported in Fig.5 and 7, where comparative representations, planar to circular, are presented in streamline-patterns and third-invariants. Then, vortex-intensity ($-\Psi_{min}$) is charted graphically in Fig.6, to be read alongside Fig.5, hence providing completion in tracking of the vortex behaviour, observed through rising flow-rate (Q/Q_0). Results are also included in Fig.5 and 6 on vortex-structures, where one can compare and contrast directly on the impact that inclusion of dissipation has caused; in the planar case, viz. adoption of conventional (Σ_{gen}^{plane}) versus proposed third-invariant ($\Sigma_{gen}^{plane-abs}$; Eq.(28)) definitions. In this data, *swIM*[L=5, λ_{D1}=0.1, β=0.9]-solutions are provided for flow-rate equivalents of $1\leq(Q/Q_0)^{\mathrm{Sim}}\leq 30$. Moreover, one notes the modest level-setting of dissipation-parameter λ_{D1}=0.1. Overall, observations can be deduced from the graphical evidence of Fig.6, in that, the circular instance is uniformly more dynamic in vortex-activity, with a sharp rise in $-\Psi_{\min}$ (terminating slope $-\Psi_{\min}$~0.4/5) gathered from $Q/Q_0\geq 4$. Equivalently, this departure point is somewhat delayed in the planar instance to $Q/Q_0\geq 10$, notably at these early rates, independent of choice on the third-invariant definition. Subsequently, the rise in vortex-intensity slope is more shallow for the conventional Σ_{gen}^{plane}-definition (terminating slope ~0.3/18), as compared to the outcome for the proposed $\Sigma_{gen}^{plane-abs}$-definition (terminating slope ~0.5/18). For example, at the largest Q/Q_0=30 recorded, this provides for extrema in planar vortex-intensities of $-\Psi_{\min}$={0.32, 0.50} on {conventional, proposed}-definitions, respectively. One refers to Fig.5 to address change in shape and orientation of the corner-vortex and its separation-line with rising flow-rate. For the *circular case*, such *concave-to-convex* adjustment in the separation-line is occurring in the interval $5\leq Q/Q_0\leq 10$; where greatest curvature is also picked-up in the vortex-intensity plot (Fig.6). Subsequent flow-rates reinforce this trend. In the corresponding *planar instance*, such adjustment appears in the interval $10\leq Q/Q_0\leq 15$ under $\Sigma_{gen}^{plane-abs}$-definition; whilst, it is barely apparent under Σ_{gen}^{plane}-definition. At around Q/Q_0=15, the jump in vortex-intensity magnitude between $\Sigma_{gen}^{plane-abs}$ and Σ_{gen}^{plane} results is practically doubled, from values $-\Psi_{\min}$~0.05 to 0.09. This trend of increase widens through the extended range $20\leq Q/Q_0\leq 30$, with extrema commented on above; and in which the outward bulge into the core flow with convex-shaped separation line is clearly prominent under $\Sigma_{gen}^{plane-abs}$-approximation. These facts render the proposed extension-rate measure $\Sigma_{gen}^{plane-abs}$ as more active than the traditional Σ_{gen}^{plane}; $\Sigma_{gen}^{plane-abs}$ appears capable of delivering relatively larger levels of extensional

deformation-rates, required to trigger viscoelastic enhanced pressure-drops and asymmetrical flow-structures observed experimentally in planar contraction flows of Boger fluids [1].

Counterpart field data on third-invariant of ***D*** and dissipation-function representation is provided in Fig.7, at three sample flow-rates Q/Q_0={1, 10, 20} and comparatively across planar to circular instances. In this, attention is centred on { $\Sigma_{gen}^{plane-abs}$, Σ_{gen}^{axi} }-definitions. In Fig.7a, the general field distributions are similar in both instances, with spread of influence rising to its extrema at the contraction plane before falling away subsequently downstream, notably peaking both at the centreline and about the corner singularity. On third-invariant of ***D*** and at Q/Q_0=10, a distinguishing feature of the planar instance is the greater penetration into the corner-vortex, and a greater dip away from the corner singularity across the flow towards the centreline. This dip is absent in the circular equivalent. Moreover, from Q/Q_0=1 to Q/Q_0=10, the planar third-invariant maxima scales from 2.41 to 15.6 units, respectively (~6 times); comparably, the position on the circular case in scaling is from 3.94 to 44.2 units, respectively (~11 times) and almost twice as large as the planar instance. This has consequences on the localisation and distribution of extensional dissipation contributions. The corresponding dissipative-functions $\phi(\dot{\varepsilon})=1+\left(\lambda_{D1}\dot{\varepsilon}\right)^2$ are provided in Fig.7b, with both $\Sigma_{gen}^{plane-abs}$ and Σ_{gen}^{axi} definitions displayed at Q/Q_0={1, 10, 20}. Between these two definitions, there is no apparent distinction in the dissipative-function at low Q/Q_0-levels, of say Q/Q_0~1; whilst at higher levels, of say Q/Q_0=10, there is almost 6 times factor of increase in $\phi(\dot{\varepsilon})$-peak, from $planar_{\max}$-$\phi(\dot{\varepsilon})$=3.42 to $circular_{\max}$-$\phi(\dot{\varepsilon})$=20.55. At Q/Q_0=20, this factor of increase becomes nearly 22. Note that with $\Sigma_{gen}^{plane-abs}$, the red-positive zone appears more squeezed up around the contraction region, when compared to its counterpart Σ_{gen}^{axi} definition.

5. ***Averaged Maxwellian single-mode relaxation-time approximation – swIM predictions***

In this section, prediction under a single-mode *swIM* model variant are displayed, with the purpose of exposing the need of further versatility required to reproduce numerically the Binding & Walters [1] experimental *epd* findings. Limitation of the *swIM* model arise through a relatively poor *epd* rising trends relative to counterpart Newtonian response, although evidence of premature oscillatory flow-regime onset at medium-to-high flow-rates is gathered as in experiments, and observed under prediction through pressure time-fluctuation.

Base solutions, swIM[L, λ_{D1}, β=0.9]-predictions; $5 \le L \le 15$, $0.5 \le \lambda_{D1} \le 0.7$.

In Table 1 with solvent-fraction β=0.9, numerical pressure-drop prediction ($\Delta P/\Delta P_0$) is reported at relative flow-rate calibrations of (Q/Q_0) of {5.5, 6.5, 7.5} units, where Q_0 is determined from the counterpart Newtonian flow-rate. These locations represent {first departure, mid-range departure, high-range departure} in ($\Delta P/\Delta P_0$) from Newtonian response. The corresponding graphical plot of such data is charted in Fig.8a, alongside stable steady-state *swIM*-model predictions. Therein one gathers, pressure-drop results for *swIM*[λ_{D1}=0.1, L=5] lie only marginally above the Newtonian reference-line. Only slight elevation is incurred with increase of the *swIM* dissipative extensional time-scale parameter (λ_{D1}) from 0.1 to 0.6. At fixed λ_{D1}=0.6, the more significant impact on pressure-drop elevation is stimulated through rise in hardening L-parameter, this being detected between results for L=5 and L=10.

Quantifying at the *first departure rate* Q/Q_0=5.5 in ($\Delta P/\Delta P_0$), the first row of Table 1 with {λ_{D1}=0.7, L=5}, there is ~2% difference against those under Newtonian equivalents. Through rise in hardening L-parameter, $\Delta P/\Delta P_0$ rises to 4% with (L={10,12,15}). In addition, at this relatively low flow-rate measure and for $0.1 \le \lambda_{D1} \le 0.7$, there is imperceptible adjustment in $\Delta P/\Delta P_0$. Upon increasing flow-rate to the *mid-range departure level* of Q/Q_0=6.5 (third row), percentage differences in ($\Delta P/\Delta P_0$) become slightly larger; being some 5% difference with (λ_{D1}=0.6, L={10,12,15}). One detects at this mid-range level of flow-rate that at the larger L-parameter setting of $12 \le L \le 15$, steady flow (for $5 \le L \le 10$) is beginning to give way to transitionary flow (star symbol notation in Table 1), a harbinger of oscillatory flow onset. This is particularly characterised at isolated zonal locations, above and downstream of the re-entrant corner, in the temporal evolution of the *pressure* variable through its time-increment relative pressure-norm, $L_2^{pressure}$, where ($10^{-6} \le L_2^{pressure} \le 10^{-5}$). On a field basis, such change would barely be perceptible under any practical measurement. Viewing the *high-range* $\Delta P/\Delta P_0$ *departure levels* together (rows 4-6), taking ($7 \le Q/Q_0 \le 8$) and with {λ_{D1}=0.5, L=5}, percentage differences remain relatively static around 2% for $7 < Q/Q_0 \le 8$. Once again, such relative percentage differences rise by some 3-4% for larger L-values, of $10 \le L \le 15$.

Adjusting solvent fraction, swIM[L=15], $0.5 \le \lambda_{D1} \le 0.8$, $0.9 \le \beta \le 0.95$*:*

Data reported in Table 2, follow on consecutively from Table 1, with the focus shifting to ($\Delta P/\Delta P_0$)-results for larger hardening L-parameter (L=15) and switch in solvent-fraction from β=0.9 to β=0.95. Again, star notation (*) is invoked on transition setting, denoting the onset of oscillatory flow ($10^{-6} \le$

$L_2^{pressure} \leq 10^{-5}$); and double-star notation (**) depicting stronger oscillatory flow conditions ($10^{-2} \leq L_2^{pressure} \leq 10^{-1}$). Clearly, as flow-rates advance and at this more elevated (L=15) setting, rising levels of λ_{D1} at fixed solvent fraction (β=0.9), provide for both transitionary and oscillatory states. Similarly, Fig.8b is the counterpart to Fig.8a, but now charts the relative trends in transitionary and oscillatory flows.

Covering the first row of ($\Delta P/\Delta P_0$)-data of Table 2 with $0.5 \leq \lambda_{D1} \leq 0.8$ and for the first departure rate Q/Q_0=5.5: solvent-fraction (β=0.9)-solutions generate stable steady-states, with 3~7% difference in ($\Delta P/\Delta P_0$) from the Newtonian value of 4.07 units. Then, upon elevation in solvent-fraction from β=0.9 to β=0.95, transitionary state is first observed for $\lambda_{D1} \geq 0.8$; whereupon pressure-drop matching is highly precise, to within 7% of the Newtonian-base value. Following Table 1 and at the *mid-range departure level* of Q/Q_0=6.5 (row 3, Table 2, target Newtonian-value 4.81 units), percentage differences in ($\Delta P/\Delta P_0$) rise from 3% with {λ_{D1}=0.5, β=0.9}, as much as 8% when approaching (λ_{D1}=0.8). Here and relative to {λ_{D1}=0.5, β=0.9}-solution, transition arises at relatively smaller λ_{D1}=0.6, 5% difference, and oscillatory state at λ_{D1}=0.8, 8% drop. Notably within oscillatory flow, when contrasting against {λ_{D1}=0.8, β=0.9}-solution, but with the larger solvent-fraction (β=0.95), ($\Delta P/\Delta P_0$) rises yet further to 5.33 units, being some 2% larger in difference from the {λ_{D1}=0.8, β=0.9}-solution. Sampling the *high-range* ($\Delta P/\Delta P_0$) *departure level* (row 5, Table 2), with Q/Q_0=7.5 and (β=0.9), variation from the Newtonian reference remains within 5-6% for $0.5 \leq \lambda_{D1} \leq 0.8$. Transition and oscillatory states gradually shift to lower λ_{D1}-values, as rates rise throughout ($7.5 \leq Q/Q_0 \leq 8$). At λ_{D1}=0.8 and for ($7.5 \leq Q/Q_0 \leq 8$), the switch in solvent-fraction from (β=0.9) to (β=0.95), stimulates a marked rise in ($\Delta P/\Delta P_0$) percentage differences of between 11~12%. So, for example, at Q/Q_0=7.5, this yields departure from the Newtonian value (5.56 units) of 11%, reaching a predicted value of (6.25 units).

Trends in solution temporal convergence are conveyed in Fig.9, furnishing the evidence to support the discussion on ($\Delta P/\Delta P_0$)-data above in Tables 1, 2 and in Fig.8. This includes steady-state, transitionary and oscillatory solution phases, as gathered under the *swIM*-model at (Q/Q_0=6.5). Plots are provided per individual solution-component, through velocity, stress, and pressure variables. Parameter settings range over $0.6 \leq \lambda_{D1} \leq 0.9$, $0.9 \leq \beta \leq 0.95$, and $5 \leq L \leq 15$; with default base-values of {λ_{D1}=0.6, β=0.9}. General flow-state categorization and points of observation are as follows. *Stable solutions* apply under (λ_{D1}=0.6), with both *swIM*[L=5] and *swIM*[L=10]; yet the former implementation supplies superior temporal-convergence behaviour in rates for all solution-components. The *transitionary phase*, to oscillatory flow conditions, arises with *swIM*[L={12, 15}, λ_{D1}=0.6], under levels of time-increment

relative component norms of $\{10^{-6} \leq L_2^{pressure} \leq 10^{-5},\ 10^{-7} \leq L_2^{velocity} \leq 10^{-6},\ 10^{-6} \leq L_2^{stress} \leq 10^{-5}\}$; notably, $L_2^{pressure}$ is always dominant. *Oscillatory flow phase* conditions are observed for *swIM*[L=15, λ_{D1}=0.8], under time-increment norms of $\{10^{-2} \leq L_2^{pressure} \leq 10^{-1},\ 10^{-4} \leq L_2^{velocity} \leq 10^{-3},\ 10^{-5} \leq L_2^{stress} \leq 10^{-4}\}$; clearly, $L_2^{pressure}$ now dominates. *Unstable solutions*, encountering intractability, are observed with *swIM*[L=15, λ_{D1}=0.9].

Anchoring flow-rate at Q=6.5, Fig.10 and 11 cover planar temporal *swIM*-traces for parameters {Q, β, L, λ_{D1}}={6.5,[0.9,0.95], [5-15], [0.6-0.9]}. Of these, Fig.10 plots individual solution-components of {pressure, velocity, stress}, at a sample-point location within the contraction-zone above the re-entrant corner. For comparison, Fig.11 provides only temporal pressure traces at a second point, located on the inlet-centreline. Four distinct flow phases are identified of {steady, transitionary, oscillatory, unstable} in the component temporal traces of Fig.10. Such fluctuation shows up strongly in both pressure and velocity, whilst only mildly in stress. In contrast at the inlet-centreline, the *temporal pressure traces* of Fig.11 again follow the four flow phases identified around the contraction zone, whilst velocity and stress traces remain unaffected by fluctuation (thus not shown). In the oscillatory phase, increase of solvent-fraction between β=0.9 and β=0.95, is noted to considerably reduce the amplitude of fluctuation. In detail and for L=15 solutions, the pressure-trace at λ_{D1}=0.6 (β=0.9) is steady-stable (smooth, non-oscillatory), at λ_{D1}=0.8 (β=[0.9,0.95]) is oscillatory, and at λ_{D1}=0.9 (β=0.95) is unstable. One notes the elevation of solvent-fraction into the unstable phase, necessary to capture these solutions.

Fig.12 and 13 include streamline-patterns and third-invariant distributions, as counterpart to Fig.10 and 11. The streamline and third-invariant of $\boldsymbol{D}$ patterns indicate that steady-stable and transitionary solutions are practically indistinguishable, {β, L, λ_{D1}}={0.9, [5-15], 0.6}. With a shift into the oscillatory phase {β, L, λ_{D1}}={[0.9, 0.95], 15, 0.8}, the salient-corner vortex strength increases some 1.5 times (Fig.12), and lack of smoothness is beginning to appear in third-invariant, particularly around and above the contraction zone (Fig.13). The unstable phase is captured, just prior to divergence, with solvent-fraction elevation, via {β, L,λ_{D1}}={0.95, 15, 0.9}. Here in Fig.12, again there is amplification in salient-corner vortex strength, but also a zoom reveals an intense vortex-cap appearing just above the re-entrant corner, this being some 10 times stronger in rotational intensity than the salient-corner vortex. This also corresponds to a sudden burst of intensity in third-invariant (extrema ~2000 units, Fig.13) about the re-entrant corner.

6. Continuous-spectrum relaxation-time function approximation – *swAM* predictions

In this section, numerical solutions with the proposed new hybrid model of *swAM* is considered to demonstrate the effective capture of enhance levels of pressure-drop and the 'bulb-flow' reported by Binding & Walters [1]. As such, for experimental pressure-drop prediction, it is necessary to adjust the m_1–parameter selection within the predictions with a solution window of m_1=[-0.01, -0.25], see Table 3 and Fig.14 with both linear and logarithmic scales. One may classify six pressure-drop data subsets (I-VI), based on the experimental pressure-drop data as shown in Fig.14a. Here, the slope of the piecewise linear-function ($m_1=a(Q/Q_0)+b$) to each pressure-drop subset is correlated against an averaged m_1-value across each Q/Q_0-range (Q/Q_0={{0,5}, {5,5.5}, {5.5,6}, {6,6.5}, {6.5,7}, {7,8}}. With the spline-slopes of a={-0.02, -0.18, -0.1, -0.1, -0.1, 0.0}, and under *swAM*-linear spline, this generates average (m_1)-values per interval and a 6-tuple of (m_1)={-0.01, -0.1, -0.15, -0.2, -0.25, -0.25} over six intervals, with the averaged m_1 factor of $m_{1-avg}=\sum_{n=6}^{i=1} m_i=-0.16$. One can gather that *swAM* six-interval spline-fit solutions match closely across all six interval rate-ranges and data-points, as desired. The rheology for such a fit is presented in Fig.4d,e. Here, the values of *swAM* spline-fit-η_e (Fig.4d) are higher than *swIM*-η_e at rates $7<\lambda_1\dot{\varepsilon}<10$ and *swAM* spline-fit-N_1^{shear} (Fig.4e) are stronger than *swIM*-N_1^{shear} at rates $\lambda_1\dot{\gamma}>7$. See also López-Aguilar *et al.* [3] for various spline-fit matching through extensional-based dissipative parameter (λ_{D1}) and (m_2)-power-index parameter. Note that, in the present study with the planar contraction flow, *swAM*(m_1, m_2=-0.2) model leads to unstable solutions. This could be due to larger extensional viscosity in comparison to *swAM*(m_1, m_2=0.0) model, see Fig.4c. Alternatively, one may adjust the level of extensional viscosity by employing different functions for $\eta_{ext}(\lambda_{D1}\dot{\varepsilon})$ or different values of λ_{D1} for viscous (λ_{D1v}) and polymeric (λ_{D1p}) parts, see Eq.(27). In the present study, λ_{D1} is taken to be the same values as λ_{D1v} and λ_{D1p} (i.e. $\lambda_{D1}=\lambda_{D1v}=\lambda_{D1p}$). Earlier experience with the circular contraction and contraction-expansion flows and the present work, have revealed that the extensional viscosity effects sustain a strong influence on pressure-drop outcome; see [2-3, 6, 8, 37]. Moreover, in Nyström *et al.* [37], a new means emerged to practically measure the extensional viscosity of Boger fluids via pressure-drop measurement for the axisymmetric hyperbolic contraction-expansion flow. There, one found a best fit to measured *epd* from predicted *epd* (simulation) to determine a material

time-constant λ_{D1} and reproduce extensional viscosity (η_E) from relationship between extensional viscosity and *epd*, a motivation for the above *swAM L*-spline fit to pressure-drop data.

The pressure-drop data in Fig.15 and Table 4 summarise the key results of this study, in the successful and beneficial use of the continuous-spectrum approximation, viz. the *swAM*–model implementation. The data is presented in comparative form to discrete-spectrum *swIM* –predictions, at parameter settings of $\{\beta,\ L,\ \lambda_{D1}\}=\{0.9,\ 10,\ 0.4\}$. One notes directly, in the election of a sub-function $\lambda_{sh}(\lambda_1\dot{\gamma})$ to represent the relaxation-time variation under the continuous-spectrum *swAM* approximation, that the necessity to elevate other parameters, such as (λ_{D1}) as under *swIM*–predictions, is now somewhat relieved (Fig.15). It becomes immediately apparent that *swAM*–predictions are well capable of capturing the target experimental excess pressure-drops, whilst retaining steady-stable solutions, and this at the modest level of dissipative parameter of (λ_{D1}=0.4). Here, the (*swAM, L*-spline, $m_1\neq 0$)-*pressure-drop*-data match closely across all interval rate-ranges with the experimental data (Fig.15). This is achieved by commencing solution search from *swIM*(λ_{D1}=0.4) form, at each flow-rate setting. One recalls that a principal reason for this is the wide choice of N_1–response, departing from the rigid FENE-CR selection of the *swIM*–alternative (see below). As such, there are significant differences from *swIM*(λ_{D1}=0.4)-pressure-drop data for all flow-rates, where *swIM*–data only track the Newtonian response (Fig.15, Table 4).

In terms of accuracy in pressure-drop prediction (see Table 4), at the relatively low flow-rate level of (Q/Q_0)=0.53 units, there is no departure in ($\Delta P/\Delta P_0$) prediction from the Binding & Walters [1] experimental data under *swIM swAM* (m_1=-0.1). At the intermediate flow-rate of (Q/Q_0)={1.7, 2.01} units, a marked underprediction (~{12, 56}%) is recorded for the single averaged *swIM* model-variant, whilst the continuous-spectrum *swAM*-model predicts experimental pressure-drop level with a minimal difference (~{0, 1}%). At the higher rate of (Q/Q_0)=6.5 *swAM1*(m_1=-0.3) and *swAM2* (m_1=-0.625) fluids depart in pressure-drop prediction capabilities, with *swAM2* matching experimental pressure-drop, whilst *swAM1* remains short with a 45% underprediction. This establishes the close quantitative agreement between the *swAM*-predictions and those of the experimental data (within 2% of target at maximum), with oscillatory flow condition. In addition, this concurs with the material properties of both *swIM* and *swAM* models, as shown in Fig.4. One refers here in particular to the higher level of extensional viscosity achieved with *swAM* at medium rates, when compared to that of *swIM*; and even stronger N_1, which is stronger still than Oldroyd-B at rates $1<\lambda_1\dot{\gamma}<20$.

With the major rheological differences between *swIM* and *swAM* models lying within N_1–representation, this is exposed in corresponding field plots of Fig.16, over a range of flow-rates, $4 \leq Q/Q_0 \leq 8$ with $\{\beta, L, \lambda_{D1}\}=\{0.9, 10, 0.4\}$. Here, one observes similar *swIM* and *swAM* trends at $Q/Q_0=4$, where pressure-drops equate. Shifting forward in flow-rate to $Q/Q_0 \geq 6.5$, larger values of N_1 are detected in *swAM*-predictions ($N_{1max}=153.9$), above and around the contraction, being some 35% larger than with *swIM*-predictions at $Q/Q_0=6.5$ ($N_{1max}=100.6$). This trend is continued to still higher flow-rates of $Q/Q_0=8$, where N_{1max} considerably strengthens. With *swAM,* there is emergence of a sharp negative N_1-peak (-204.4 units) around the wall-location at the re-entrant corner vicinity; proving almost 13 times larger than that with *swIM* (-15.9 units). On positive extrema, *swAM* N_1-max is 468.7 units, whilst it is 135.1 units under *swIM,* some 3.5 times lower in peak-value. Similar factor differences (4 times across models) are observed upstream along the wall, which is consistent with N_1^{shear} data of Fig.4b.

There are some interesting new vortex-dynamics to explore with *swAM*($\lambda_{D1}=0.4$, $m_1=-0.25$)-predictions, as flow-rate rises into fresh territory, above and beyond $Q/Q_0=10$ units (Fig.17). All four flow phases of {steady-stable, transitionary, oscillatory, unstable} are identified via the attendant temporal norm plots. Steady numerical solutions are predicted up to $Q/Q_0=10$ (Fig.17a), at which limit a lip-like vortex first appears (*lv*, $\psi_{min}=-0.0011$), proving one order of magnitude lower than its salient-corner counterpart (*scv*, $\psi_{min}=-0.01147$). This lip-like vortex is not detected at $Q/Q_0=9$, for example. Transitionary flow applies for $10.5 \leq (Q/Q_0) \leq 11$ (Fig.17b), switching to oscillatory flow for $11.5 \leq (Q/Q_0) < 12$ (Fig.17c), becoming unstable ~ $Q/Q_0=12$ (encountering solution divergence through temporal evolution). On entering the transitionary flow phase (Fig.17b), the lip-like vortex resembles a bulbous shape (as reported in Binding and Walters 1988 [1]), that is growing with Q/Q_0-rise and dominating the salient-corner vortex, which itself is now shrinking accordingly. At $Q/Q_0=10.5$, *lv*-intensity is ~6 times larger than that of the salient-corner vortex; at $Q/Q_0=11$, this factor rises to ~ 13 times larger. In the oscillatory phase at $Q/Q_0=11.5$, *lv*-intensity is ~24 times larger than *scv*-intensity. This trend continues into the unstable phase at $Q/Q_0=12$, and just prior to temporal divergence, where *lv*-intensity is ~33 times larger than *scv*-intensity.

In Fig.18, an expanded range of flow-rates is interrogated, made accessible to steady-stable solution states by decreasing the dissipative parameter (λ_{D1}), from $\lambda_{D1}=0.4$ to $\lambda_{D1}=0.2$. Hence and for *swAM*{β, L, λ_{D1}, m_1}={0.9, 10, 0.2, -0.25}, one can detect the gradual switch-over in domination of vortex-intensity, from *lip-vortex* to *elastic-corner vortex*. At $Q/Q_0=10$, *svc*-intensity ($\psi_{min}=-0.07798$) is ~24 times larger

than *lv*-intensity (ψ_{min}=-0.00329); by Q/Q_0=11, the position is almost balanced; beyond and for $Q/Q_0 \geq 12$, the pattern for λ_{D1}=0.4 of Fig.17 is recovered for ($10 \leq (Q/Q_0) \leq 14$), with *lv*-intensity rising and *scv*-intensity falling. The transitionary phase is now encountered at Q/Q_0~13 (*lv*-intensity 60 times *scv*-intensity), and the oscillatory phase $Q \geq 14$ (*lv*-intensity two orders-of-magnitude larger than *svc*-intensity). The upper reaches of flow-rate solutions of Q/Q_0=15 and Q/Q_0=17, still retain oscillatory character, whereupon at Q/Q_0=15 one is able to observe a single large elastic-corner vortex, such that the dominant bulging lip-vortex has subsumed the receding salient-corner vortex, with its tell-tale convex-concave shaped vortex separation-line highly prominent. From Q/Q_0=15 to Q/Q_0=17, the elastic-corner vortex intensity has now doubled in strength, and the vortex separation-line adopts a fairly uniform convex-shape. The corresponding vortex-intensity trends with rising flow-rate are charted in Fig.19 for both *swAM*(λ_{D1}=0.4) and *swAM*(λ_{D1}=0.2). This information identifies the construction of salient-corner vortices (*scv*), the emergence of lip-vortices (*lv*) and the appearance of the 'bulb flow' structure reported by Binding and Walters 1988 [1], to finalise in the establishment of elastic-corner-vortices (*ecv*). Here, one may detect the reduction in *scv*-intensity with lip-vortex appearance, when anticipating vortex-growth with increasing flow-rate.

7. Conclusions

This study has achieved its principal objective, as set out. That is, through the use of the continuous-spectrum relaxation-time function approximation and its *swAM* implementation, the experimentally determined enhanced pressure-drops of some planar contraction flows with Boger fluids have now been captured (Binding & Walters [1]). This has revealed the rheological dependencies in achieving this goal, in particular via extensional viscosity and first normal-stress difference properties. In addition, the systematic approach taken has demonstrated the threshold nature of some of the solutions discussed, as they pass between steady-stable, transitionary, oscillatory to unstable flow states. A key aspect of achieving enhanced pressure-drops in planar contractions at high flow-rates has been in a reformulation of strain-rate invariants. Counterpart flow dynamics also mirror experimental observation. The use of a continuous-spectrum relaxation-time function in the constitutive model has also permitted greater flexibility in control of first normal-stress difference response that has in turn lead to steady-stable solutions, which may not have been possible to extract otherwise.

Declaration of Competing Interest

The authors declare that they have no conflict of interest

Acknowledgments

This work was scheduled to be presented by the first author, late Professor Mike Webster, as an *invited Keynote Lecture* in the special session for *SJ Lee* at the 7th Pacific Rim Conference on Rheology (PRCR2018), Jeju Island, S. Korea, June 2018. Sincere thanks must be expressed to the many helpful contributions made to this study through our colleagues in the INNFM Wales, but particularly to Professor Ken Walters FRS and Professor Peter Townsend. Support from Consejo Nacional de Ciencia y Tecnología (CONACYT, Mexico), from UNAM (Mexico) under the projects PAIP 5000-9172 and PAPIIT IA105818, and from Prof. Nithiarasu, Deputy Head of College of Engineering and Director of Research, Swansea University, UK, are gratefully acknowledged.

Appendix: Scaling and boundary conditions (Planar vs circular)

By imposing the following boundary conditions for the planar and circular configurations, fully developed outflow conditions are established ensuring no change in streamwise and vanishing cross-stream kinematics. One may derive the flow-rates in terms of averaged velocity (U^{avg}) by integrating the rates of flow through whole cross-section:

	Planar	circular
Boundary condition (exit profiles)	$U^{p}_{exit}(y) = U_{\max}(y-3)(5-y)$	$U^{A}_{exit}(r) = U_{\max}(1-r^2)$
Flow-rate	$Q^{p}_{exit} = 2\int_{\xi=0}^{\xi=1}\int_{y=3}^{y=4} U_{\max}(y-3)(5-y)d\xi dy$	$Q^{A}_{exit} = \int_{0}^{2\pi}\int_{r=0}^{r=1} U^{A}_{\max}(1-r^2)rdrd\theta$
Flow-rate in terms of U^{avg}	$Q^{p}_{exit} = 2.U^{avg}_{p}.1^2 = 2.\left(\frac{2}{3}\right)U_{\max}$	$Q^{A}_{exit} = U^{avg}_{A}.\pi.1^2 = \frac{\pi}{2}U^{A}_{\max}$

Consequently, one could establish a relationship between Weissenberg numbers for the planar and circular configurations by assuming the same flow-rates (Q) for both configurations ($Q^{p}_{exit} = Q^{A}_{exit}$), then $\frac{U^{avg}_{p}}{\pi} = \frac{U^{avg}_{A}}{2}$ and $Wi_p = \frac{\pi}{2}Wi_A$. The similar line of argument may be adopted if assuming the same averaged velocity (U^{avg}) for both planar and circular ($U^{avg}_{p} = U^{avg}_{A}$). So, per unit area $\frac{Q^{p}_{exit}}{2} = \frac{Q^{A}_{exit}}{\pi}$ and $Wi_p = Wi_A$.

References

[1] D.M. Binding, K. Walters, On the use of flow through a contraction to estimating the extensional viscosity of mobile polymer solutions", J. Non-Newton. Fluid Mech. 30 (1988) 233-250.

[2] J.E. López-Aguilar, M.F. Webster, H.R. Tamaddon-Jahromi, M. Pérez-Camacho, O. Manero, Contraction-ratio variation and prediction of large experimental pressure-drops in sharp-corner circular contraction-expansions - Boger fluids, J. Non-Newton. Fluid Mech. 237 (2016) 39-53.

[3] J.E. López-Aguilar, M.F. Webster, H.R. Tamaddon-Jahromi, O. Manero, D.M. Binding, K. Walters, On the use of continuous spectrum and discrete-mode differential models to predict contraction-flow pressure drops for Boger fluids, Phys. Fluids 29 (2017) 121613.

[4] I.E. Garduño, H.R. Tamaddon-Jahromi, M.F. Webster, The falling sphere problem and capturing enhanced drag with Boger fluids, J. Non-Newton. Fluid Mech. 231 (2016) 26–48.

[5] I.E. Garduño, H.R. Tamaddon-Jahromi, M.F. Webster, Flow past a sphere: Predicting enhanced drag with shear-thinning fluids, dissipative and constant shear-viscosity models, J. Non-Newton. Fluid Mech., 244 (2017) 25–41.

[6] H.R. Tamaddon-Jahromi, J.E. López-Aguilar, M.F. Webster, On modelling viscoelastic flow through abrupt circular 8:1 contractions – matching experimental pressure-drops and vortex structures, J. Non-Newton. Fluid Mech. 251 (2018) 28-42.

[7] J.E. López-Aguilar, M.F. Webster, H.R. Tamaddon-Jahromi, K. Walters, Numerical vs experimental pressure drops for Boger fluids in sharp-corner contraction flow, Phys. Fluids 28 (2016) 103104.

[8] H.R. Tamaddon-Jahromi, I.E. Garduño, J.E. López-Aguilar, M.F. Webster, Predicting Excess pressure drop (*epd*) for Boger fluids in expansion-contraction flow, J. Non-Newton. Fluid Mech. 230 (2016) 43–67.

[9] J.E. López-Aguilar, M.F. Webster, H.R. Tamaddon-Jahromi, O. Manero, High-Weissenberg predictions for micellar fluids in contraction-expansion flows, J. Non-Newton. Fluid Mech., 222 (2015) 190–208.

[10] J.P. Rothstein, G.H. McKinley, The axisymmetric contraction-expansion: the role of extensional rheology on vortex growth dynamics and the enhanced pressure drop, J. Non-Newton. Fluid Mech. 98 (2001) 33-63.

[11] S. Nigen, K. Walters, Viscoelastic contraction flows: comparison of axisymmetric and planar configurations, J. Non-Newton Fluid Mech. 102 (2002) 343-359.

[12] M.S.N. Oliveira, P.J. Oliveira, F.T. Pinho, M.A. Alves, Effect of contraction ratio upon viscoelastic flow in contractions: The axisymmetric case, J. Non-Newton. Fluid Mech. 147 (2007) 92–108.

[13] R.I. Tanner, *Engineering Rheology*, Second edition. Oxford University Press, Oxford, 2000.

[14] R.G. Owens, T.N. Phillips, *Computational Rheology*, Imperial College Press, London. 2002.

[15] K. Walters, M.F. Webster, The distinctive CFD challenges of computational rheology, Inter. J. Numer. Meth. Fluids, 43 (2003) 577-596.

[16] M. Aboubacar, M.F. Webster, A cell-vertex finite volume/element method on triangles for abrupt contraction viscoelastic flows, J. Non-Newton. Fluid Mech. 98(2-3) (2001) 83-106.

[17] M. Aboubacar, H. Matallah, H.R. Tamaddon-Jahromi, M.F.Webster, Numerical prediction of extensional flows in contraction geometries: hybrid finite volume/element method, J. Non-Newton. Fluid Mech. 104 (2002) 125–164.

[18] M.A. Alves, P.J. Oliveira, F.T. Pinho, On the effect of contraction ratio in viscoelastic flow through abrupt contractions, J. Non-Newton. Fluid Mech. 122 (2004) 117-130.

[19] T.N. Phillips, A.J. Williams. Comparison of creeping and inertial flow of an Oldroyd B fluid through planar and axisymmetric contractions, J. Non-Newton. Fluid Mech. 108 (2002) 25-47.

[20] R.E. Evans, K. Walters, Flow characteristics associated with abrupt changes in geometry in the case of highly elastic liquids, J. Non-Newton. Fluid Mech. 20 (1986) 11–29.

[21] D.V. Boger, D.U. Hur, R.J. Binnington, Further observations of elastic effects in tubular entry flows, J. Non-Newton. Fluid Mech. 20 (1986) 31-49.

[22] D.M. Binding, M.A. Couch, K. Walters, The pressure dependence of the shear and elongational properties of polymer melts, J. Non-Newton. Fluid Mech. 79(2–3) (1998) 137–155.

[23] J.P. Rothstein, G.H. McKinley, Extensional Flow of a Polystyrene Boger Fluid through a 4:1:4 Axisymmetric Contraction-Expansion, J. Non-Newton. Fluid Mech. 86 (1-2) (1999) 61-88.

[24] R. Keunings, A survey of computational rheology, *Edited by Binding et al., 13th International Congress on Rheology, BSR*, (2000), 7-14.

[25] R. Keunings, Micro-Macro Methods for the Multiscale Simulation of Viscoelastic Flow using Molecular Models of Kinetic Theory. In: Binding et al. (Ed.), Rheology Review, (2004) 67-98.

[26] A. Ammar, B. Mokdad, F. Chinesta, R. Keunings, A new family of solvers for some classes of multidimensional partial differential equations encountered in kinetic theory modeling of complex fluids, J. Non-Newton. Fluid Mech. 139 (2006) 153–176.

[27] A. Ammar, D. Ryckelynck, F. Chinesta, R. Keunings, On the reduction of kinetic theory models related to finitely extensible dumbbells, J. Non-Newton. Fluid Mech. 134 issues 1-3, (2006) 136-147.

[28] T.C.B. McLeish, R.G. Larson, Molecular constitutive equations for a class of branched polymers: The pom-pom polymer, J. Rheol. 42 (1998) 81–110.

[29] M.D. Chilcott, J.M. Rallison, Creeping flow of dilute polymer solutions past cylinders and spheres, J. Non-Newton Fluid Mech. 29 (1988) 381-432.

[30] J.L. White, A.B. Metzner, Development of constitutive equations for polymeric melts and solutions, J. Appl. Polym. Sci. 7 (1963) 1867-1889.

[31] J.E. López-Aguilar, M.F. Webster, H.R. Tamaddon-Jahromi, O. Manero, Convoluted models and high-Weissenberg predictions for micellar thixotropic fluids in contraction–expansion flows, J. Non-Newton. Fluid Mech. 232 (2016) 55–66.

[32] D.M. Binding *"Some personal thoughts"*, 25th Alpine Rheology Meeting, Les Gets, France, January (2013).

[33] M.F. Webster, H.R. Tamaddon-Jahromi, M. Aboubacar, Transient viscoelastic flows in planar contractions, J. Non-Newton. Fluid Mech. 118 (2004) 83–101.

[34] P. Wapperom, M.F. Webster, A second-order hybrid finite-element/volume method for viscoelastic flows, J. Non-Newton. Fluid Mech. 79 (1998) 405-431.

[35] M.F. Webster, H.R. Tamaddon-Jahromi, M. Aboubacar, Time-Dependent Algorithms for Viscoelastic Flow: Finite Element/Volume Schemes, Numer. Meth. Par. Diff. Equ. 21 (2005) 272-296.

[36] B. Debbaut, M.J. Crochet, Extensional Effects in Complex Flows, J. Non-Newton. Fluid Mech. 30 (2-3) (1988) 169-184.

[37] M. Nyström, H.R. Tamaddon Jahromi, M. Stading, M.F. Webster, Extracting extensional properties through excess pressure drop estimation in axisymmetric contraction and expansion flows for constant shear-viscosity, extension strain-hardening fluids, Rheol. Acta, 55 (2016) 373–396.

Table & figure captions

Table 1. Base solvent fraction: Numerical pressure-drop prediction ($\Delta P/\Delta P_0$) vs Newtonian values, with flow-rate (Q/Q_0) increase; *swIM* model, planar, $\{\beta, L, \lambda_{D1}\}=\{0.9, [5\text{-}15], [0.5\text{-}0.7]\}$; steady and transition to oscillatory flow. Values in brackets (in red) indicate percentage increase in ($\Delta P/\Delta P_0$) to Newtonian equivalent

Q/Q_0	Newtonian ($\Delta P/\Delta P_0$)	Numerical predictions ($\Delta p/\Delta p_0$)				
		L=5	L=10	L=12	L=15	
5.5	4.07	(2%) 4.16	(4%) 4.24	(4%) 4.26	(4%) 4.26	λ_{D1}=0.7
6.0	4.44	(2%) 4.54	(4%) 4.63	(5%) 4.66	(5%) 4.66*	
6.5	4.81	(2%) 4.92	(5%) 5.05	(5%) 5.08*	(5%) 5.08*	λ_{D1}=0.6
7.0	5.19	(2%) 5.31	(5%) 5.48	(6%) 5.50*	(6%) 5.51*	
7.5	5.56	(2%) 5.68	(5%) 5.87	(6%) 5.89*	(6%) 5.89*	λ_{D1}=0.5
8.0	5.93	(2%) 6.07	(6%) 6.29	(6%) 6.31*	(6%) 6.29*	

* Transitionary flow (L_2^{pressure} -norm on pressure, $10^{-6} \leq L_2^{\text{pressure}} \leq 10^{-5}$)

Table 2. Solvent fraction increment: Numerical pressure-drop prediction ($\Delta P/\Delta P_0$) vs Newtonian values, with flow-rate (Q/Q_0) increase; *swIM* model, planar, $\{\beta, L, \lambda_{D1}\}=\{[0.9,0.95], 15, [0.5- 0.8]\}$; transition to oscillatory flow. Values in brackets (in red) indicate percentage increase in ($\Delta P/\Delta P_0$) to Newtonian equivalent

Q/Q_0	Newtonian ($\Delta P/\Delta P_0$)	**Numerical predictions ($\Delta p/\Delta p_0$)**				
		λ_D=0.5, β=0.9	λ_D=0.6, β=0.9	λ_D=0.7, β=0.9	λ_D=0.8, β=0.9	λ_D=0.8, β=0.95
5.5	4.07	(3%) 4.18	(3%) 4.19	(4%) 4.26	(5%) 4.27*	7%) 4.37*
6.0	4.44	(3%) 4.57	(5%) 4.66*	(5%) 4.66*	(5%) 4.67*	(6%) 4.73**
6.5	4.81	(3%) 4.94	(5%) 5.08*	(5%) 5.08*	(8%) 5.25**	(10%) 5.33**
7.0	5.19	(4%) 5.38	(6%) 5.51*	(6%) 5.54*	(6%) 5.51**	(12%) 5.88**
7.5	5.56	(6%) 5.89*	(5%) 5.86*	(5%) 5.85*	(6%) 5.91**	(11%) 6.25**
8.0	5.93	(6%) 6.29*	(5%) 6.27*	(9%) 6.54**	(6%) 6.33**	(12%) 6.77**

* Transitionary flow (L_2^{pressure} -norm on pressure, $10^{-6} \leq L_2^{\text{pressure}} \leq 10^{-5}$)

** Oscillatory flow conditions ($10^{-2} \leq L_2^{\text{pressure}} \leq 10^{-1}$)

Table 3. Numerical pressure-drop prediction ($\Delta P/\Delta P_0$) vs Newtonian values, flow-rate (Q/Q_0) increase, *swIM* vs *swAM* model, planar, $\{\beta, L, \lambda_{D1}\}=\{0.9, 10, 0.4\}$, stable flow conditions, Values in brackets (in red) indicate the percentage increase in ($\Delta P/\Delta P_0$) to Newtonian equivalent.

Q/Q_0	Newtonian ($\Delta P/\Delta P_0$)	**Numerical predictions ($\Delta p/\Delta p_0$)**		
		swIM λ_{D1}=0.4	*swAM*(m_1), λ_{D1}=0.4	*swAM*(m_1), λ_{D1}=0.2
5.5	4.07	(2%) 4.16	(8%) 4.43 (m_1=-0.1)	(6%) 4.32 (m_1=-0.1)
6.0	4.44	(2%) 4.53	(12%) 5.07 (m_1=-0.15)	(10%) 4.92 (m_1=-0.15)
6.5	4.81	(2%) 4.91	(17%) 5.79 (m_1=-0.2)	(16%) 5.75 (m_1=-0.2)
7.0	5.19	(2%) 5.29	(21%) 6.56 (m_1=-0.25)	(20%) 6.46 (m_1=-0.25)
7.5	5.56	(2%) 5.66	(21%) 7.08 (m_1=-0.25)	(20%) 6.98 (m_1=-0.25)
8.0	5.93	(2%) 6.04	(22%) 7.63 (m_1=-0.25)	(21%) 7.52 (m_1=-0.25)

Table 4. Experimental pressure-drop vs numerical prediction, flow-rate $(Q/Q_0)^{Exp}$ increase, *swIM* vs *swAM* model, planar, $\{\beta, L\}=\{0.9, 10\}$, $\{\lambda_{D1}\}=\{0.2, 0.6\}$ stable flow conditions, Values in brackets (in red) indicate the percentage differences with the pressure-drop experimental data.

Q/Q_0	Binding & Walters Exp. Data[1] ($\Delta P/\Delta P_0$)	Numerical predictions ($\Delta p/\Delta p_0$)		
		swIM λ_{D1}=0.2	*swAM1*(m_1), λ_{D1}=0.2	*swAM2*(m_1), λ_{D1}=0.2
0.53	0.15	(0%) 0.15	(0%) 0.15 (m_1=-0.05)	(0%) 0.15 (m_1=-0.05)
1.7	0.52	(-12%) 0.46	(0%) 0.52 (m_1=-0.4)	(0%) 0.52 (m_1=-0.0.4)
3.3	2.01	(-56%) 0.88	(-1%) 1.98 (m_1=-0.725)	(-1%) 1.98 (m_1=-0.725)
6.5	5.53	(-67%) 1.83	(-45%) 3.02 (m_1=-0.3)	(2%) 5.66* (m_1=-0.625) ← λ_{D1}=0.6

* Oscillatory flow conditions ($10^{-2} \leq L_2^{pressure} \leq 10^{-1}$)

Table 5. Alternative measures for I_3-planar case

1) $I_3^{plane} = \left[(\boldsymbol{D}:\boldsymbol{D}) + 2\det(\boldsymbol{D}_{xy}) \right]$, where $(\boldsymbol{D}:\boldsymbol{D}) = trace(\boldsymbol{D}_{xy})^2 = \left(\frac{\partial u_x}{\partial x}\right)^2 + \left(\frac{\partial u_y}{\partial y}\right)^2 + 2\dot{\gamma}^2$, $\det(\boldsymbol{D}_{xy}) = \frac{\partial u_x}{\partial x}\frac{\partial u_y}{\partial y} - \dot{\gamma}^2$.	Lack of shear component in I_3, low values of third invariants [$O(10^{-2}$-$10^{-3})$] above the contraction zone, and $O(10^{-5}$-$10^{-6})$ in the vicinity of symmetry line (pure extension)	
2) $I_3^{plane} = 0.5\left[(\boldsymbol{D}:\boldsymbol{D}) - 2\dot{\gamma}^2 \right]$	Lack of shear component in I_3	
3) $I_3^{plane} = \frac{\partial u_x}{\partial x}\frac{\partial u_y}{\partial y} - \dot{\gamma}^2$	Lacking in inhomogeneous complex flow in shear and extension with a choice of $\Sigma_{gen}^{plane} = \sqrt[3]{4 I_3^{plane}}$ Debbaut and Crochet [36]	Numerically unstable for medium-high flow-rates ($Q/Q_0 \geq 9.0$)

Binding and Walters, JNNFM (1988)

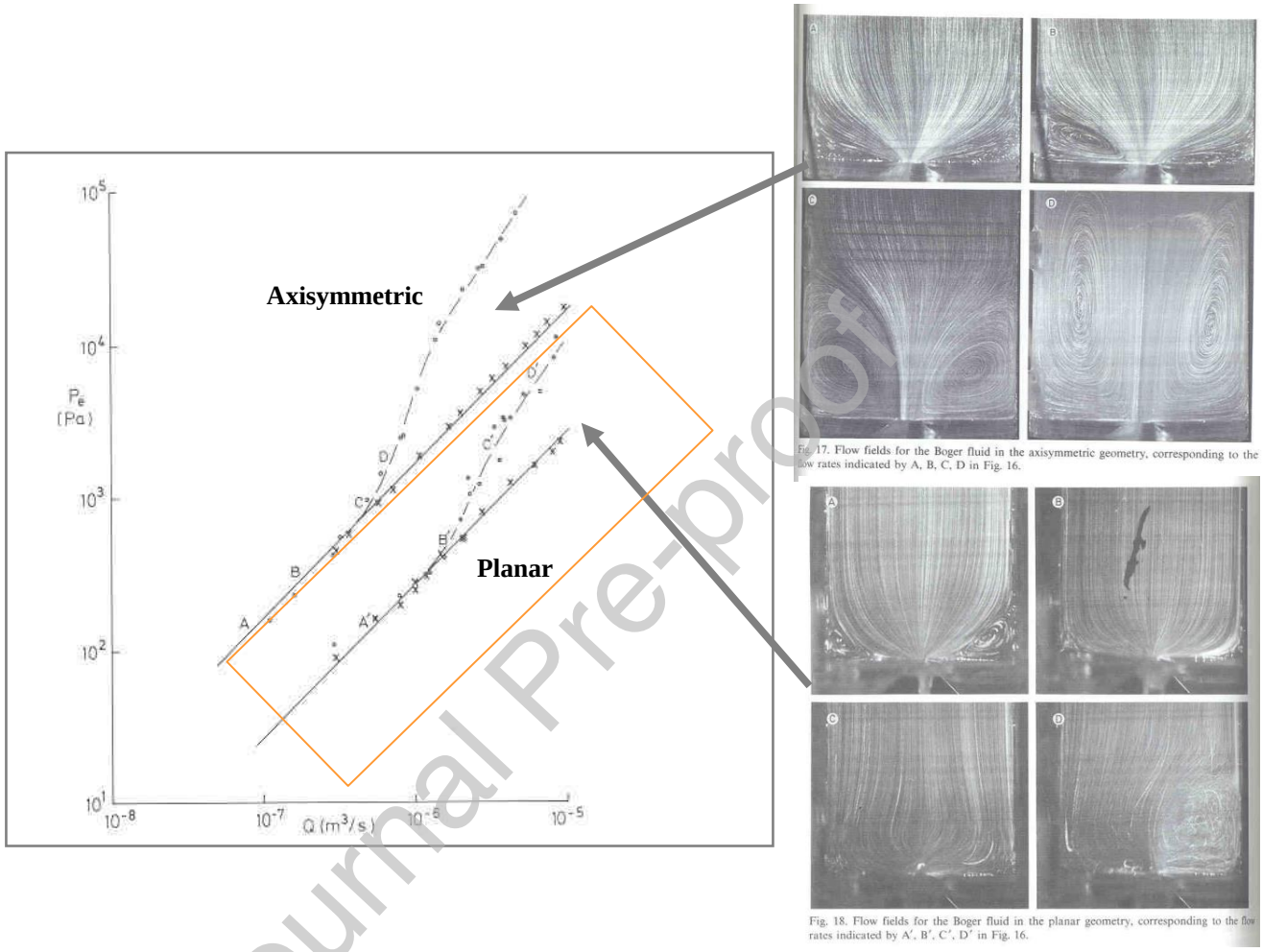

Fig. 17. Flow fields for the Boger fluid in the axisymmetric geometry, corresponding to the flow rates indicated by A, B, C, D in Fig. 16.

Fig. 18. Flow fields for the Boger fluid in the planar geometry, corresponding to the flow rates indicated by A′, B′, C′, D′ in Fig. 16.

Fig. 1. Entry pressure data and Flow fields for the Boger fluid, axisymmetric and planar contraction geometries, (from Binding and Walters [1]); the points A', B', C', D' correspond to flow rates of 0.53, 1.7, 3.3 and 6.5 mL/s respectively in the planar geometry.

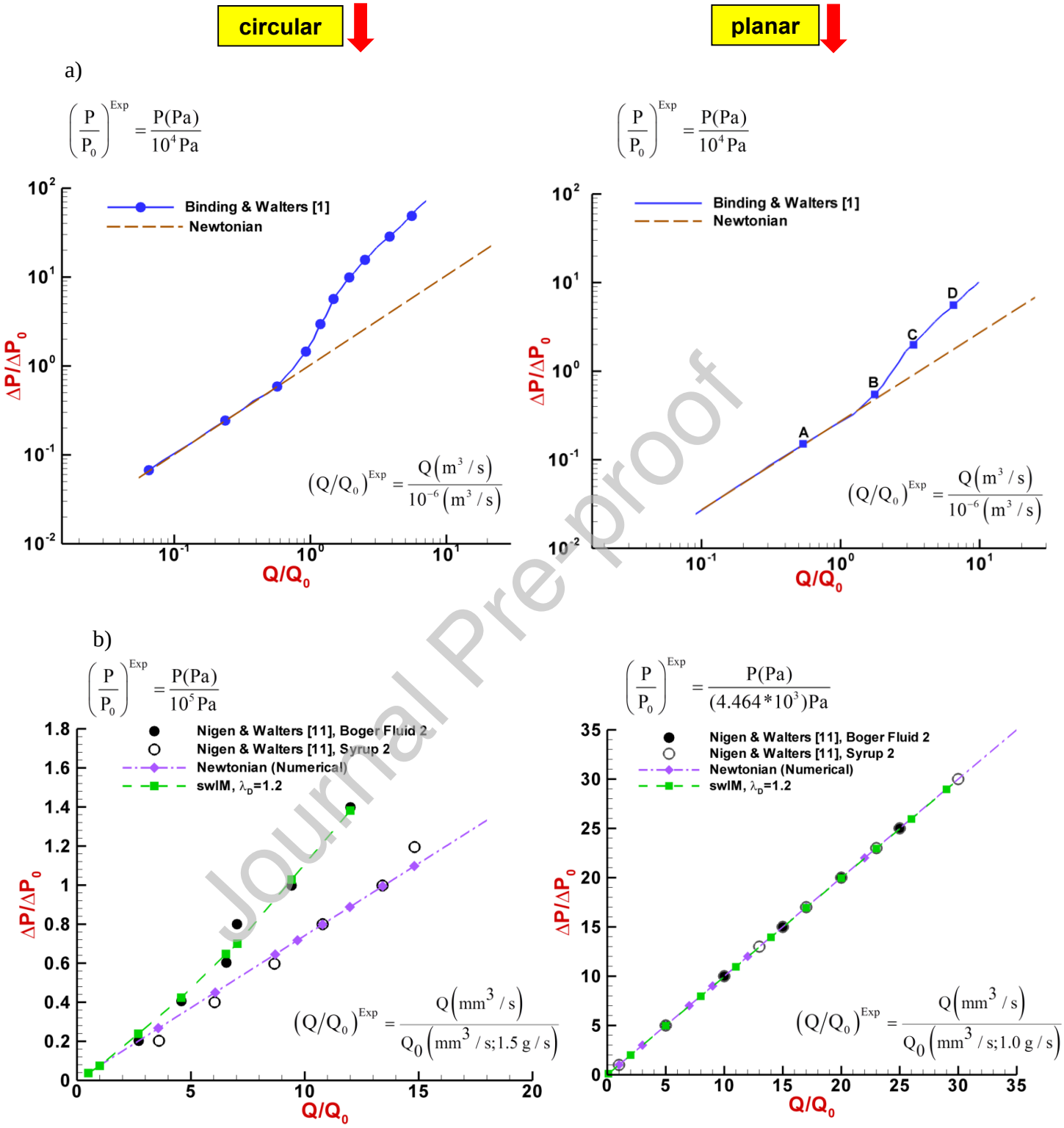

Fig. 2. a) Binding and Walter [1] experimental data; *Planar* and *axisymmetric* contractions (logarithmic scale), the points A, B, C, D correspond to non-dimensional flow rates of 0.53, 1.7, 3.3 and 6.5 mL/s, respectively in the planar geometry; b) Pressure-drop vs flow-rate, Nigen and Walters [11] 4:1 experimental vs swIM(λ_{D1}=1.2) model [López-Aguilar *et al.2016*].

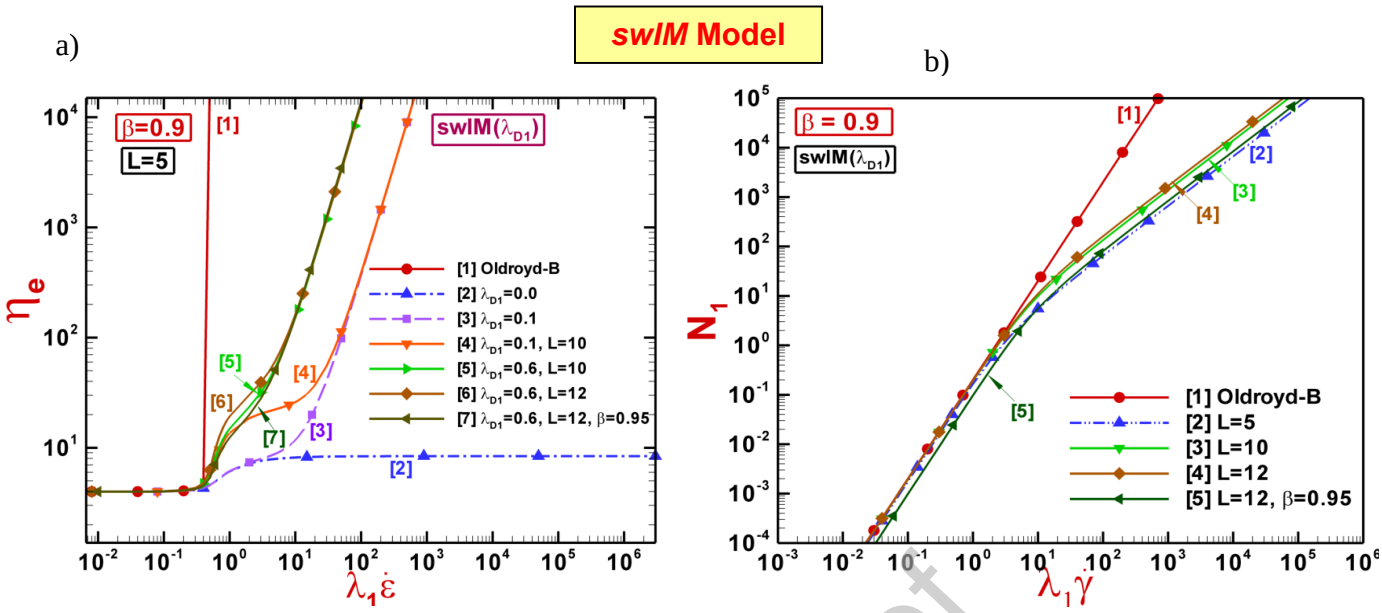

Fig. 3. a) Planar extensional viscosity and b) first normal stress difference, Oldroyd-B, *swIM* model; { β, L,λ_{D1}}={0.9, [5-12], [0.0–0.6]}

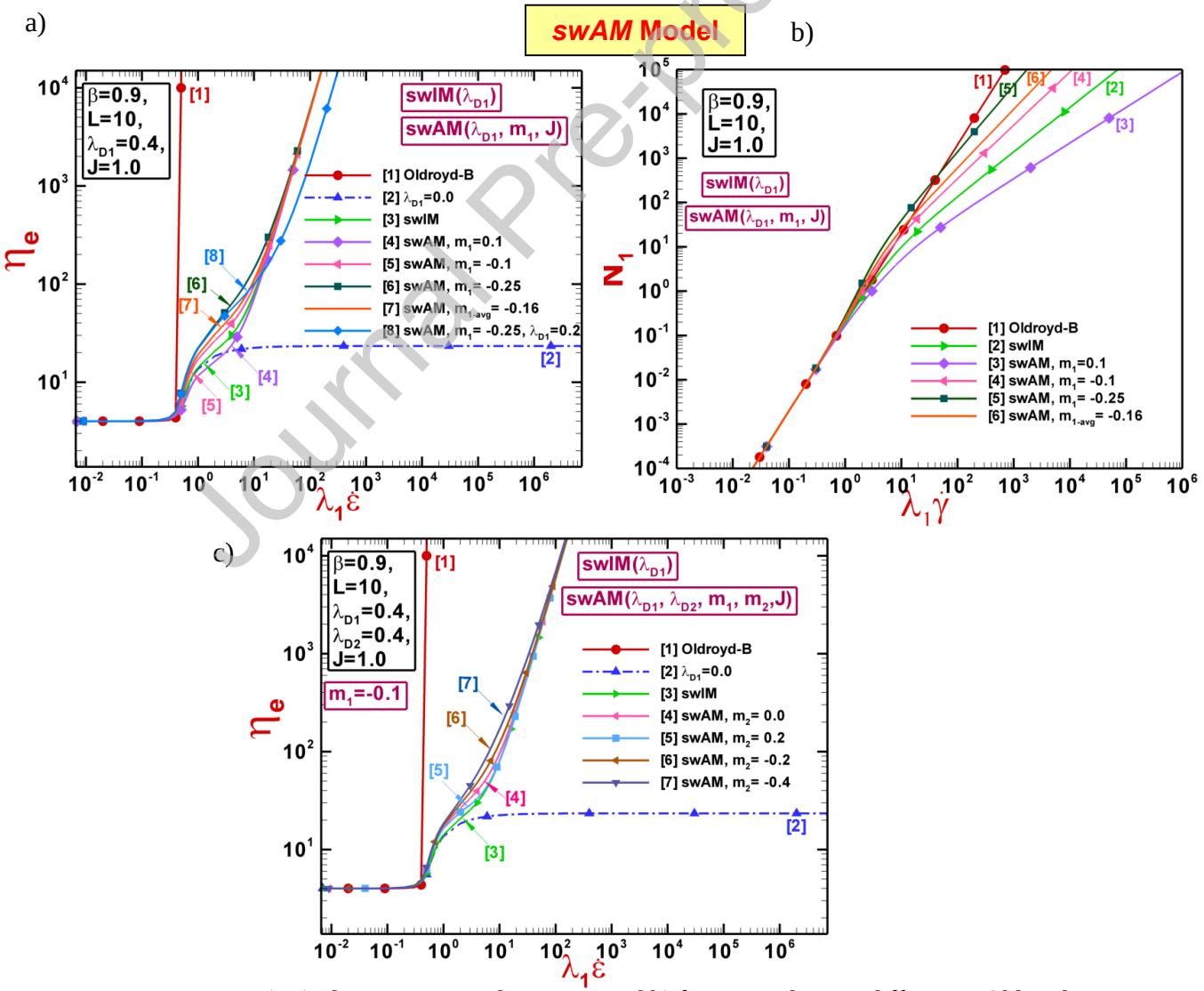

Fig. 4. a), c) Planar extensional viscosity and b) first normal-stress difference, Oldroyd-B, *swIM* and *swAM* models; {β, L, λ_{D1}}={0.9, 10, 0.4}

d)

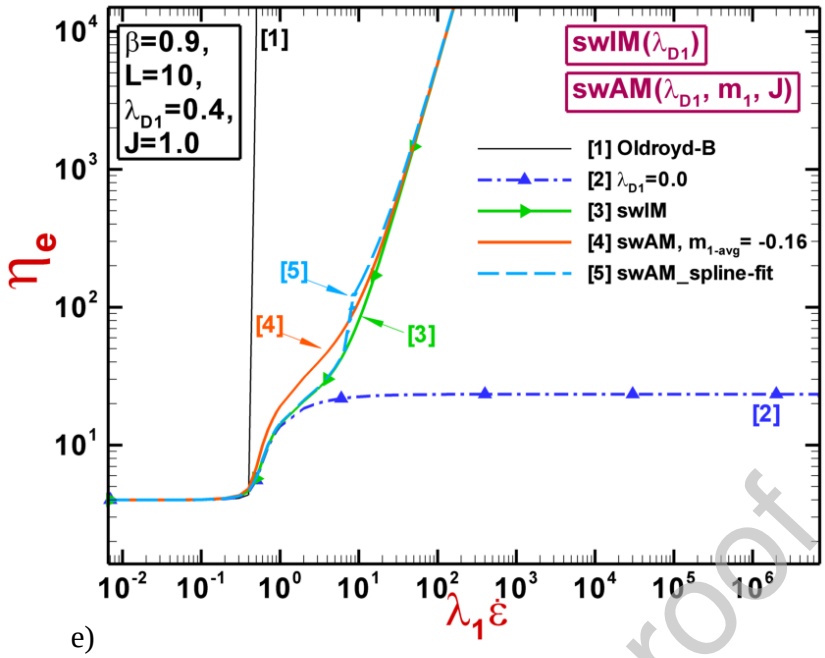

e)

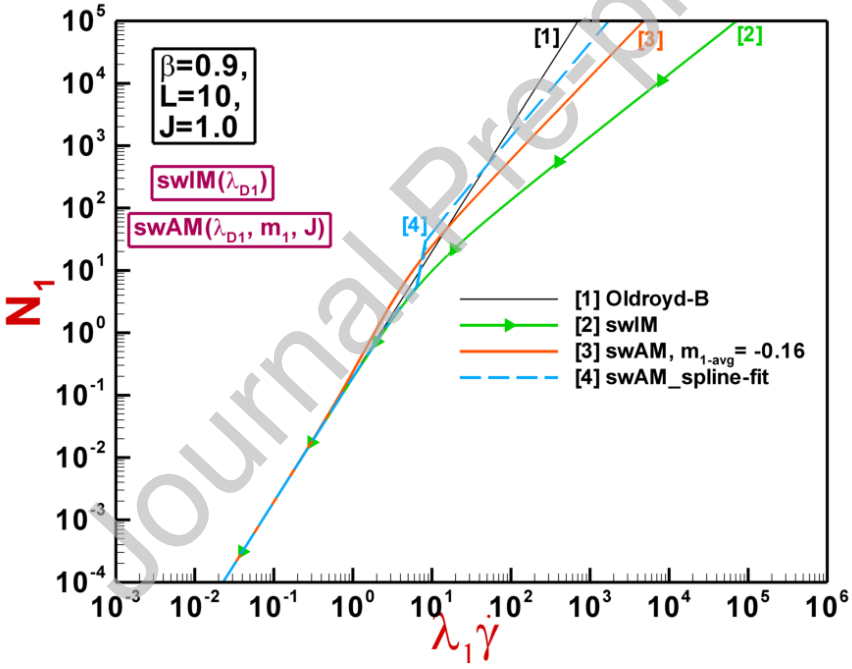

Fig. 4. d) Planar extensional viscosity and e) first normal-stress difference, Oldroyd-B, *swIM* and *swAM* (spline-fit) models; $\{\beta, L, \lambda_{D1}\}=\{0.9, 10, 0.4\}$

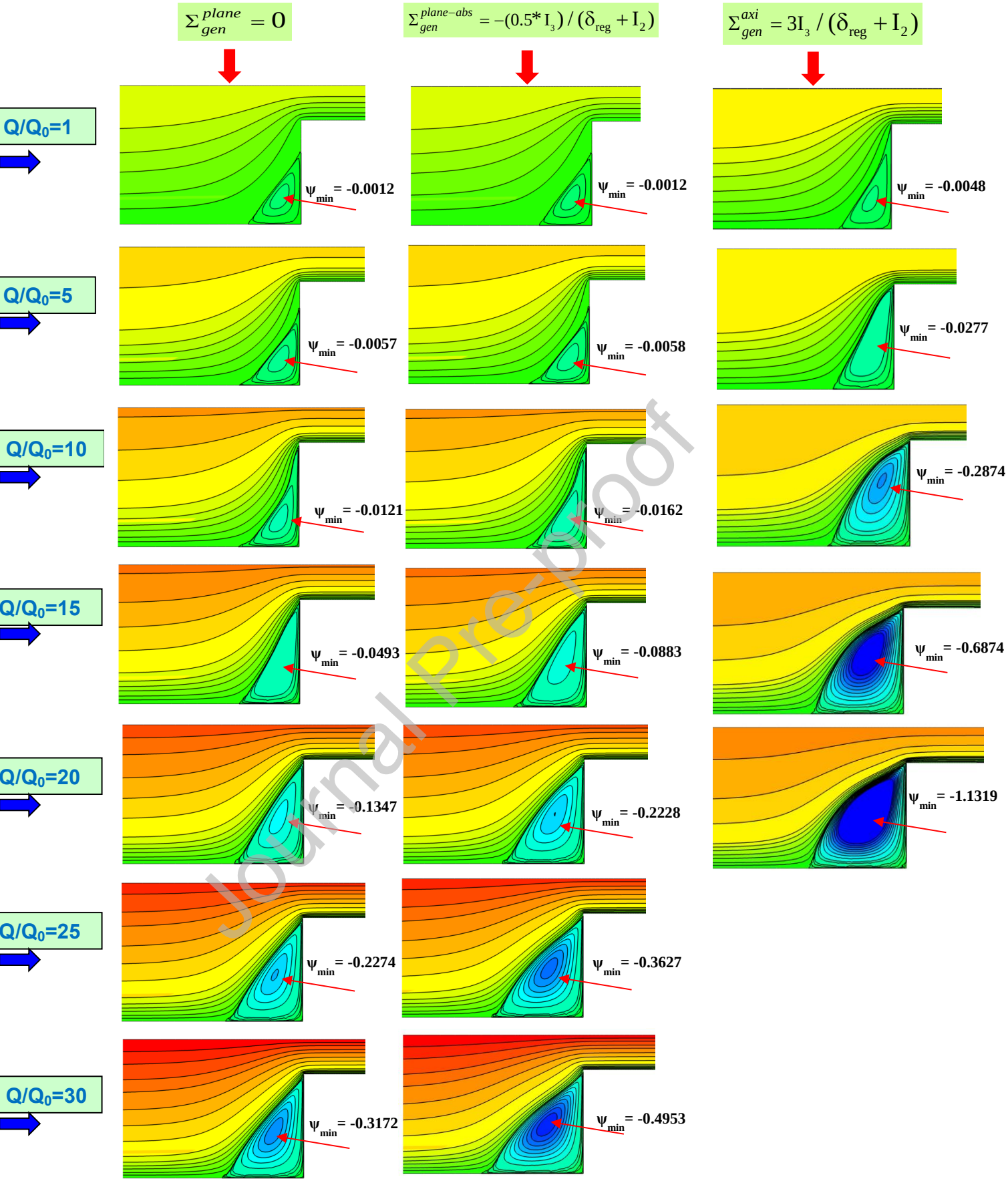

Fig. 5. Streamlines, Σ_{gen}^{plane} vs $\Sigma_{gen}^{plane-abs}$, $1 \leq (Q/Q_0) < 30$, *swIM*[L=5, λ_{D1}=0.1, β=0.9]; planar vs circular

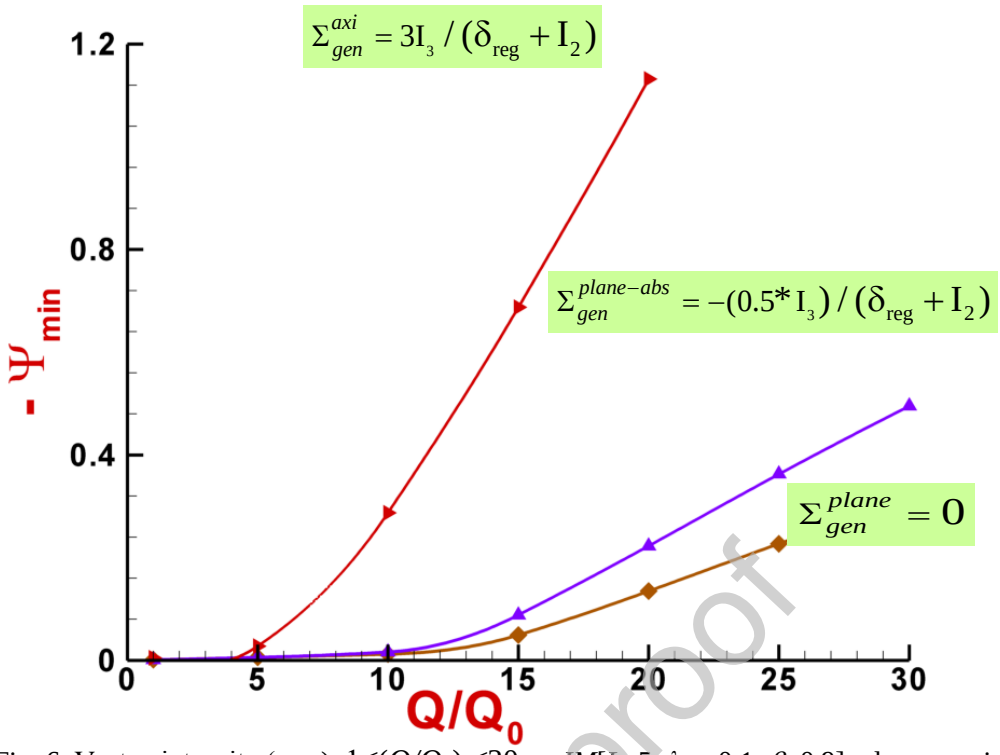

Fig. 6. Vortex intensity (ψ_{min}), $1 \leq (Q/Q_0) \leq 30$, *swIM*[L=5, λ_{D1}=0.1, β=0.9]; planar vs circular

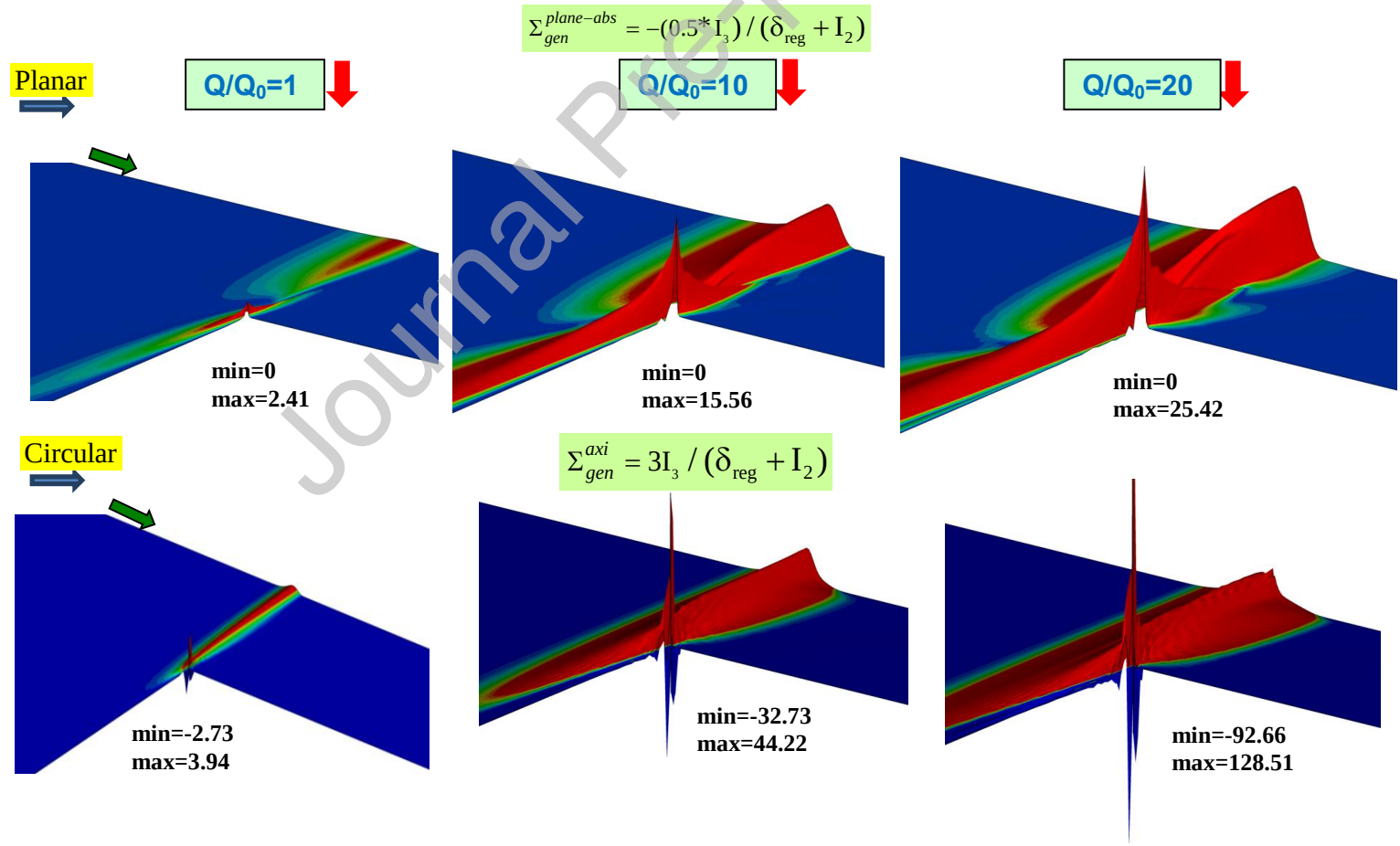

Fig. 7a. Third-invariant fields, (Q/Q_0)= 1, 10, 20 units, *swIM*[L=5, λ_{D1}=0.1, β=0.9], planar vs circular

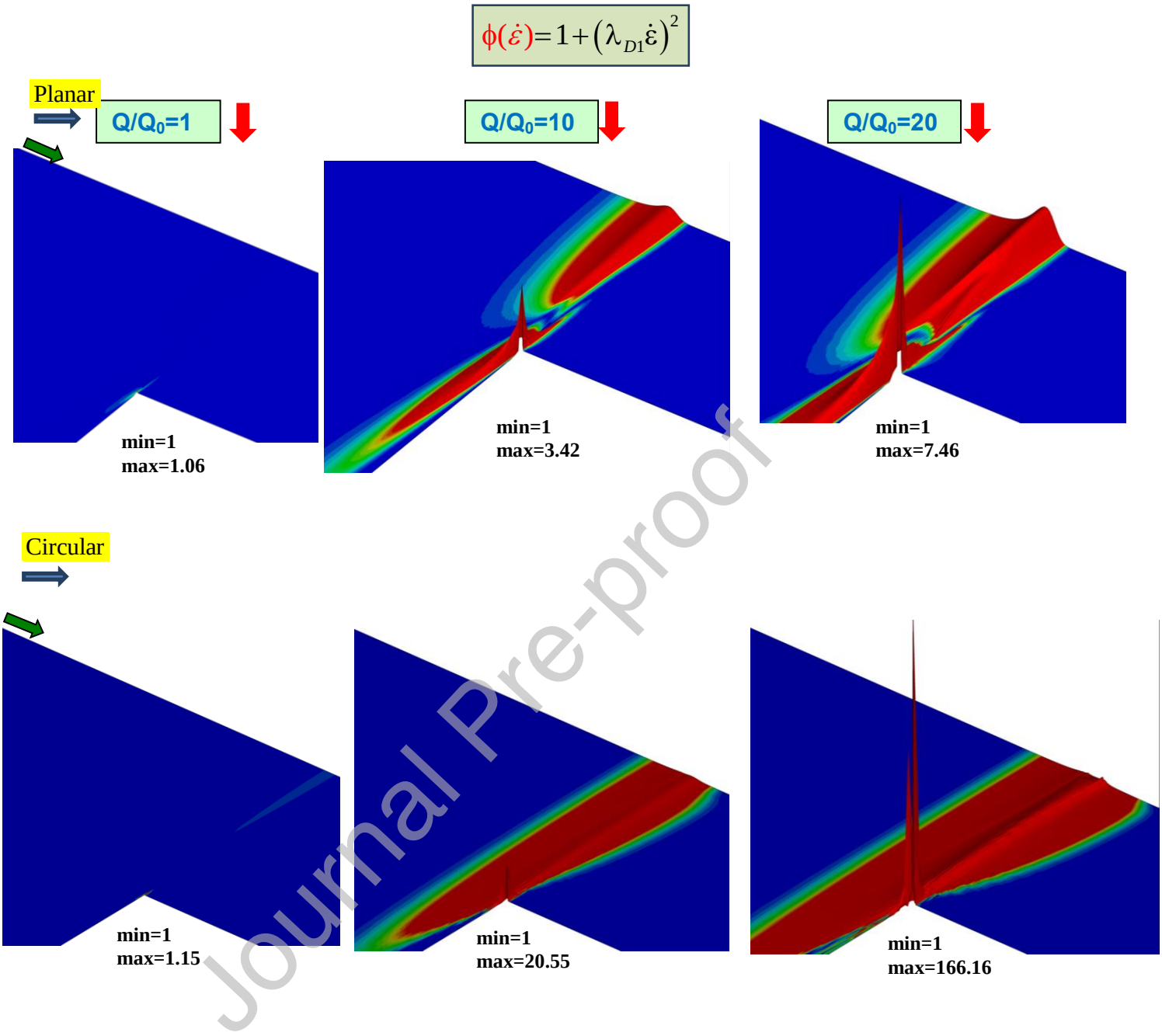

Fig. 7b. $\phi(\dot{\varepsilon})=1+(\lambda_{D1}\dot{\varepsilon})^2$, (Q/Q_0)= 1, 10, 20 units, *swIM*[L=5, λ_{D1}=0.1, β=0.9], planar vs circular

a)

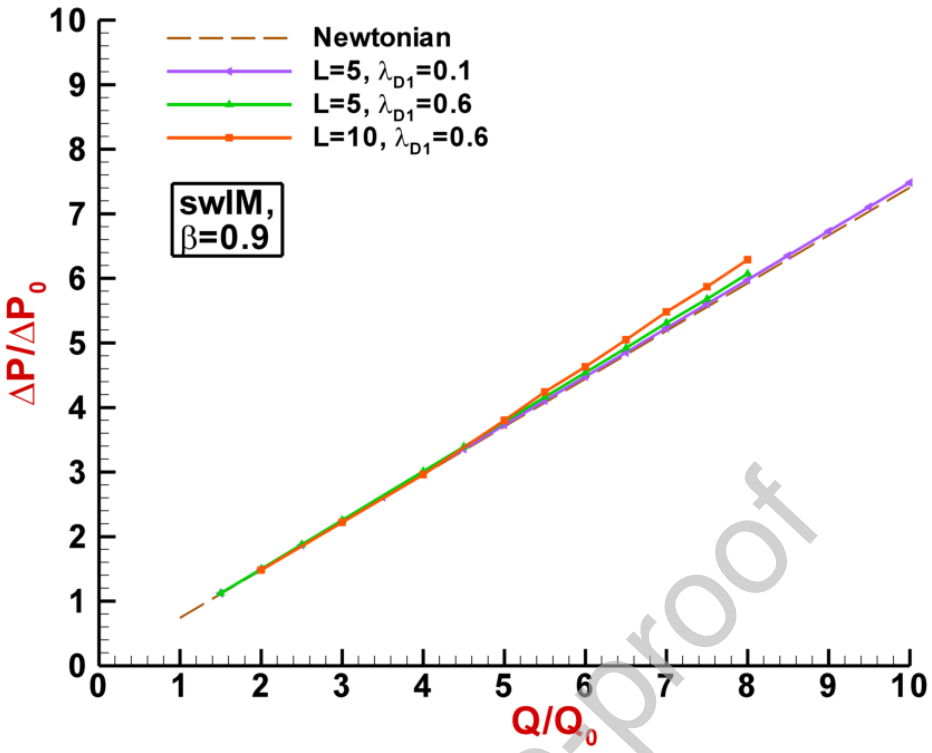

b)

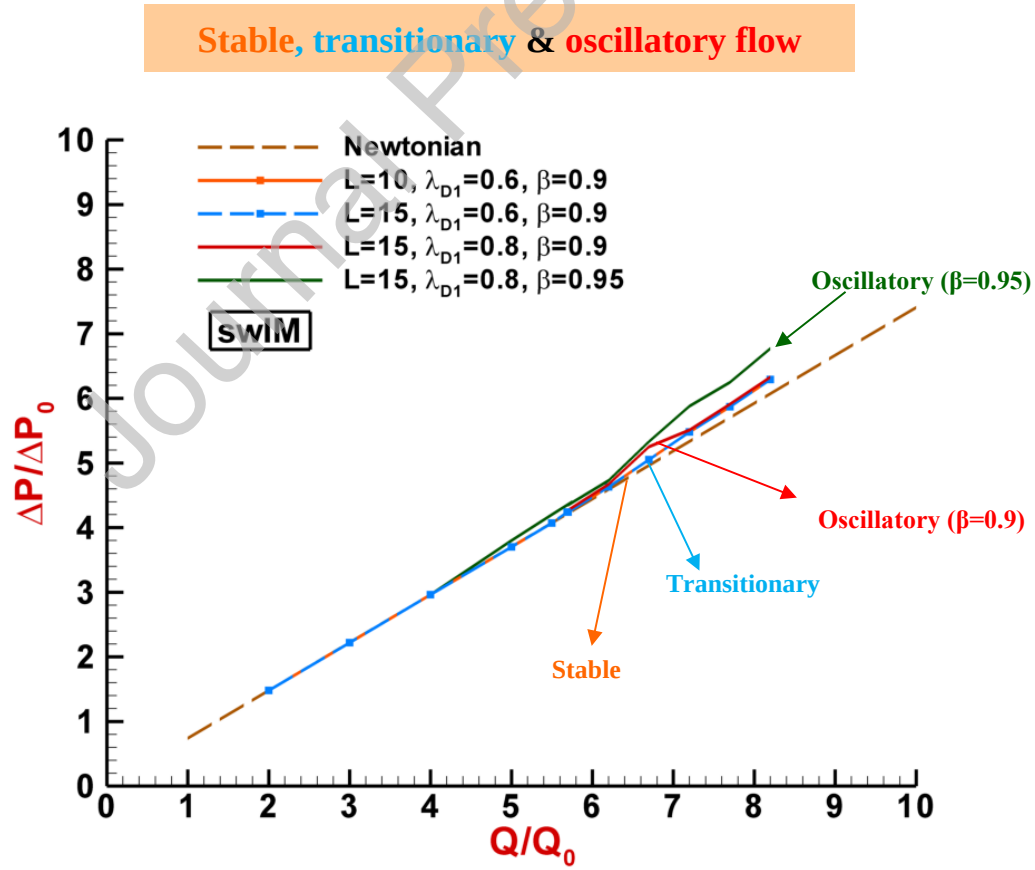

Fig. 8. Pressure-drop vs (Q/Q_0), *swIM* model, a) Steady flow condition, b) Transitionary and oscillatory flow conditions, linear scale

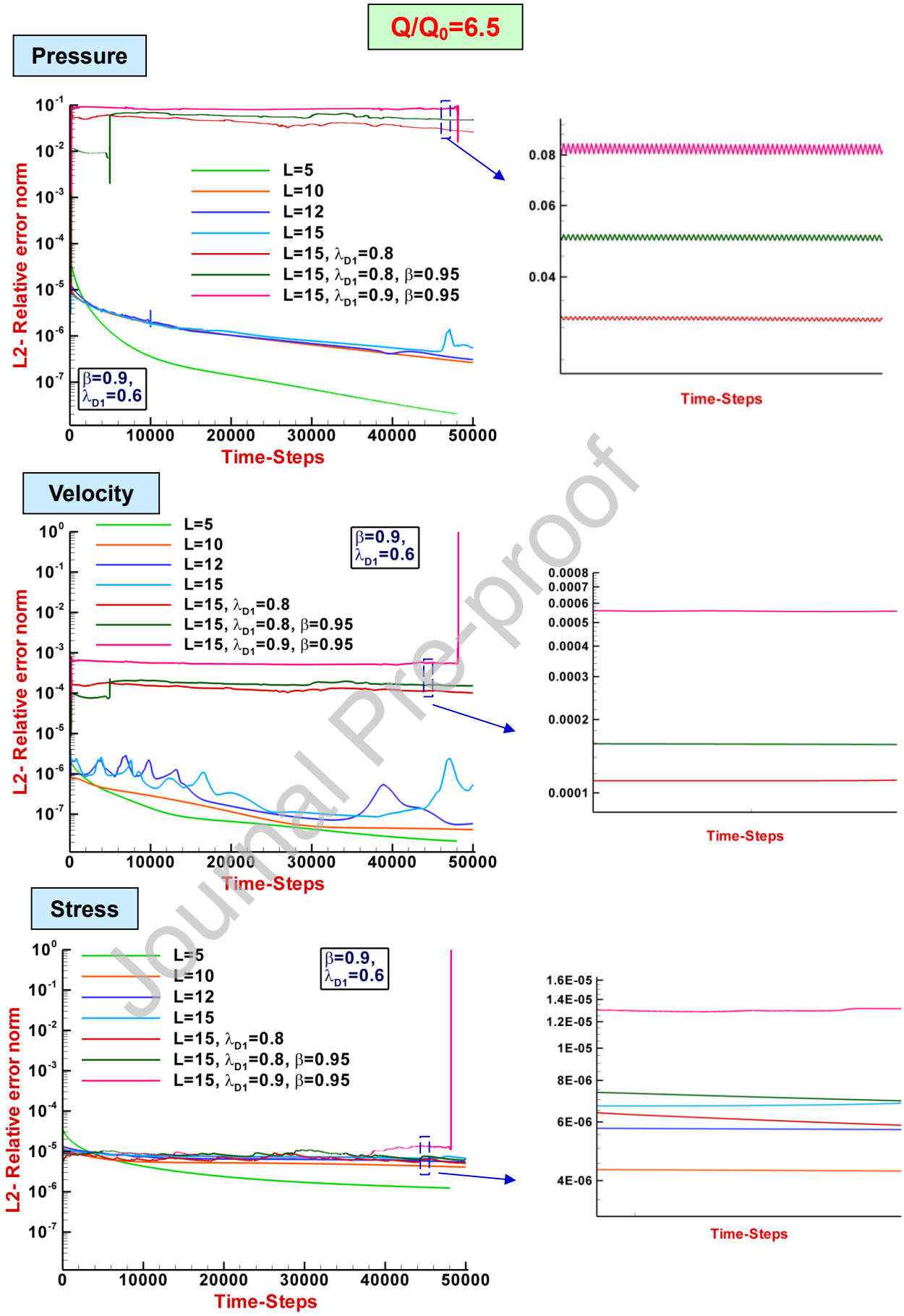

Fig. 9. Temporal convergence plots, *swIM* model;
{(Q/Q_0), β, L,λ_{D1}}={6.5,[0.9,0.95], [5-15], [0.6-0.9]}

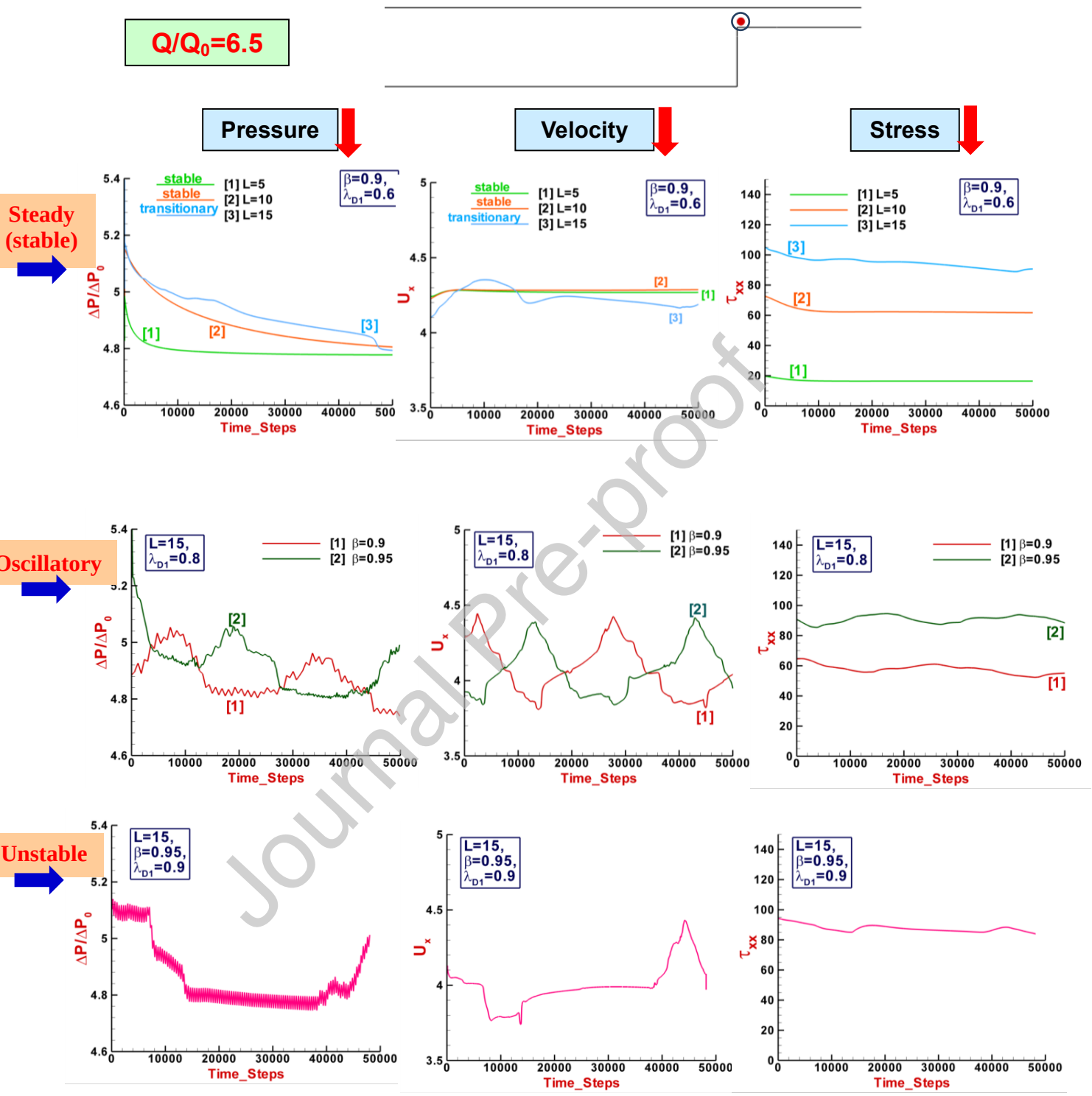

Fig. 10. Temporal component development, contraction zone; *swIM* model;
{(Q/Q_0), β, L,λ_{D1}}={6.5,[0.9,0.95], [5-15], [0.6-0.9]}

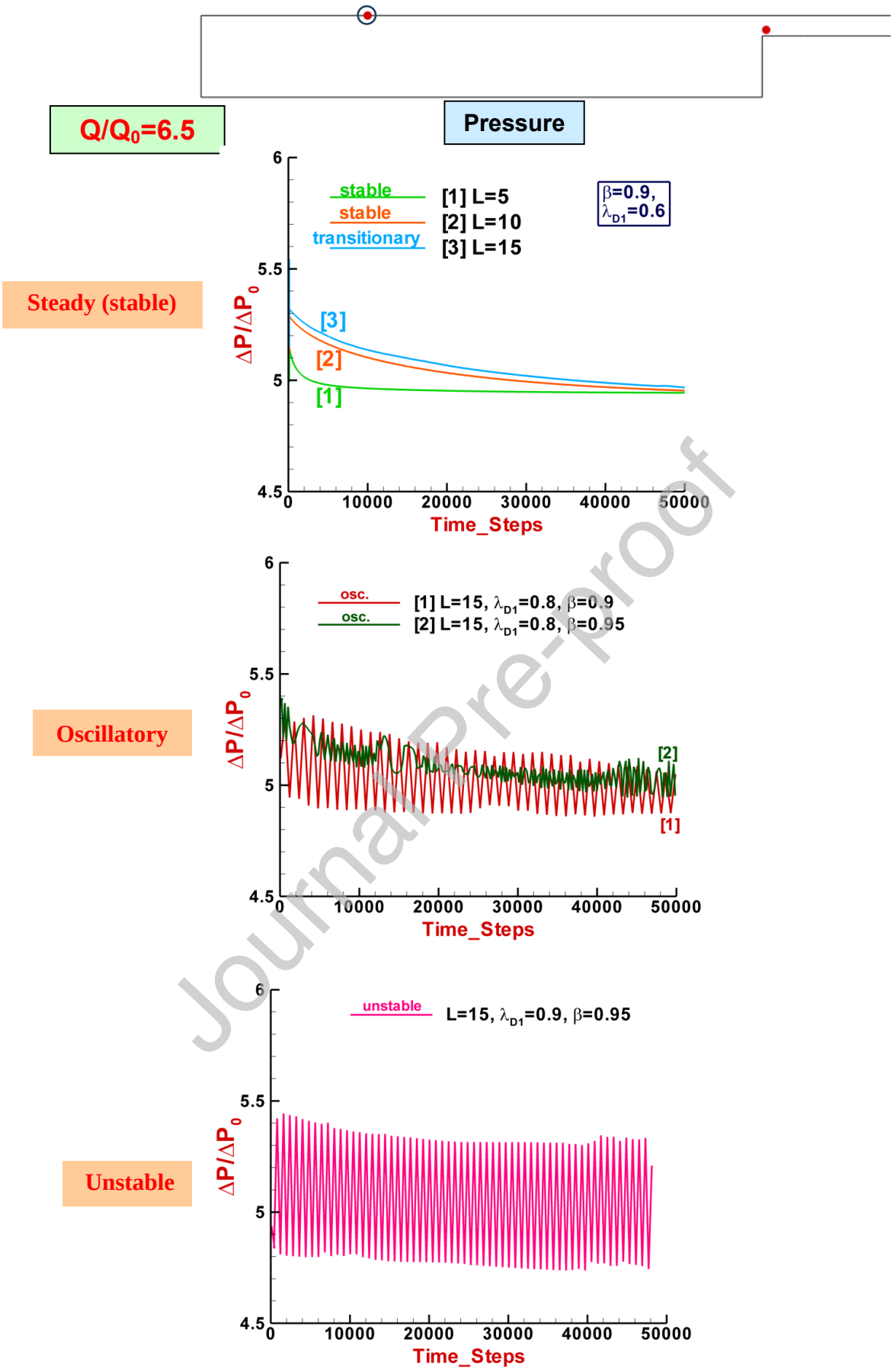

Fig. 11. Temporal pressure development, inlet centreline; *swIM* model; $\{(Q/Q_0)^{Exp}, \beta, L, \lambda_{D1}\}=\{6.5,[0.9,0.95], [5\text{-}15], [0.6\text{-}0.9]\}$

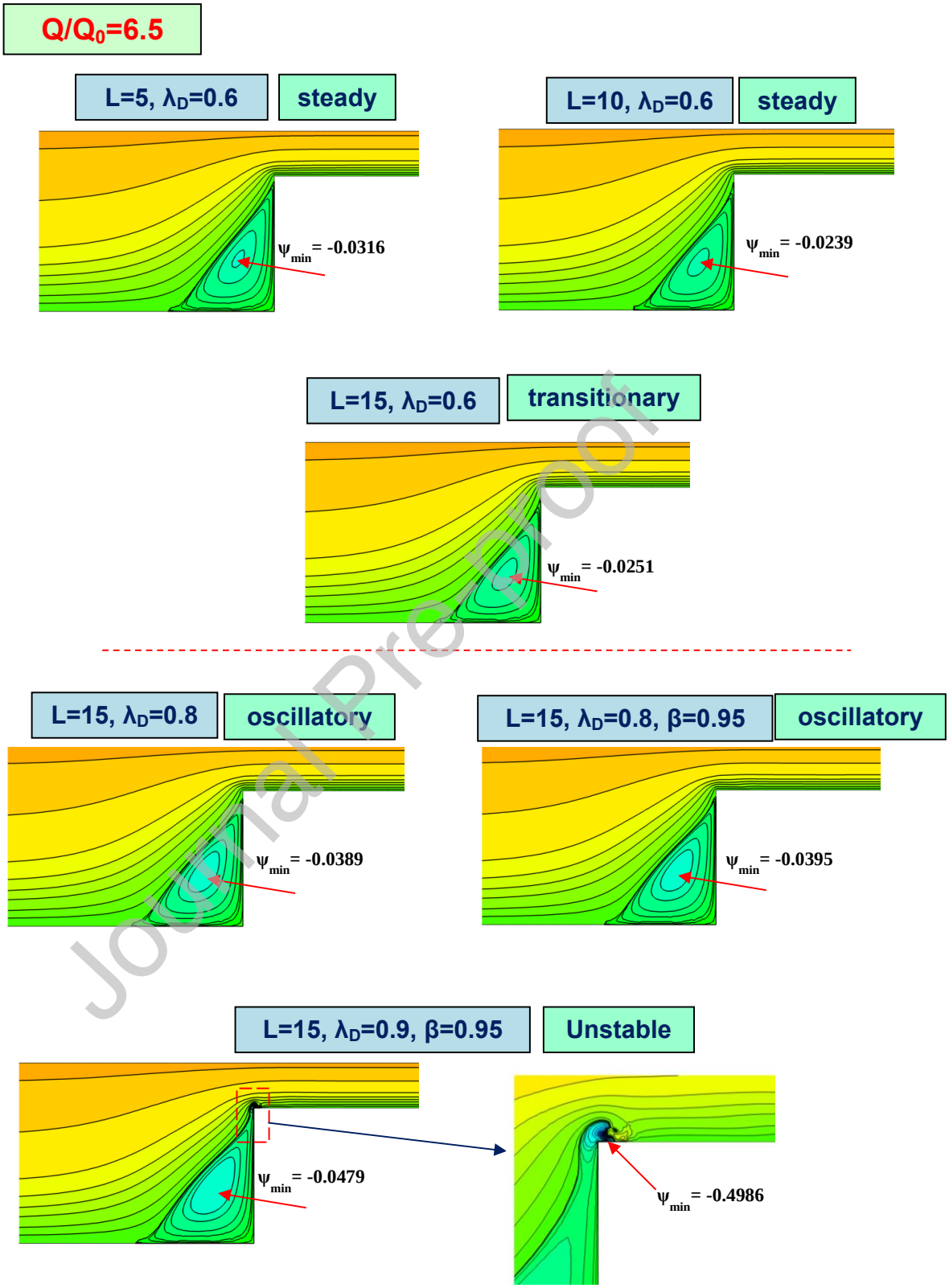

Fig. 12 Streamlines, *swIM* model; {(Q/Q_0), β, L,λ_{D1}}={6.5,[0.9,0.95], [5-15], [0.6-0.9]

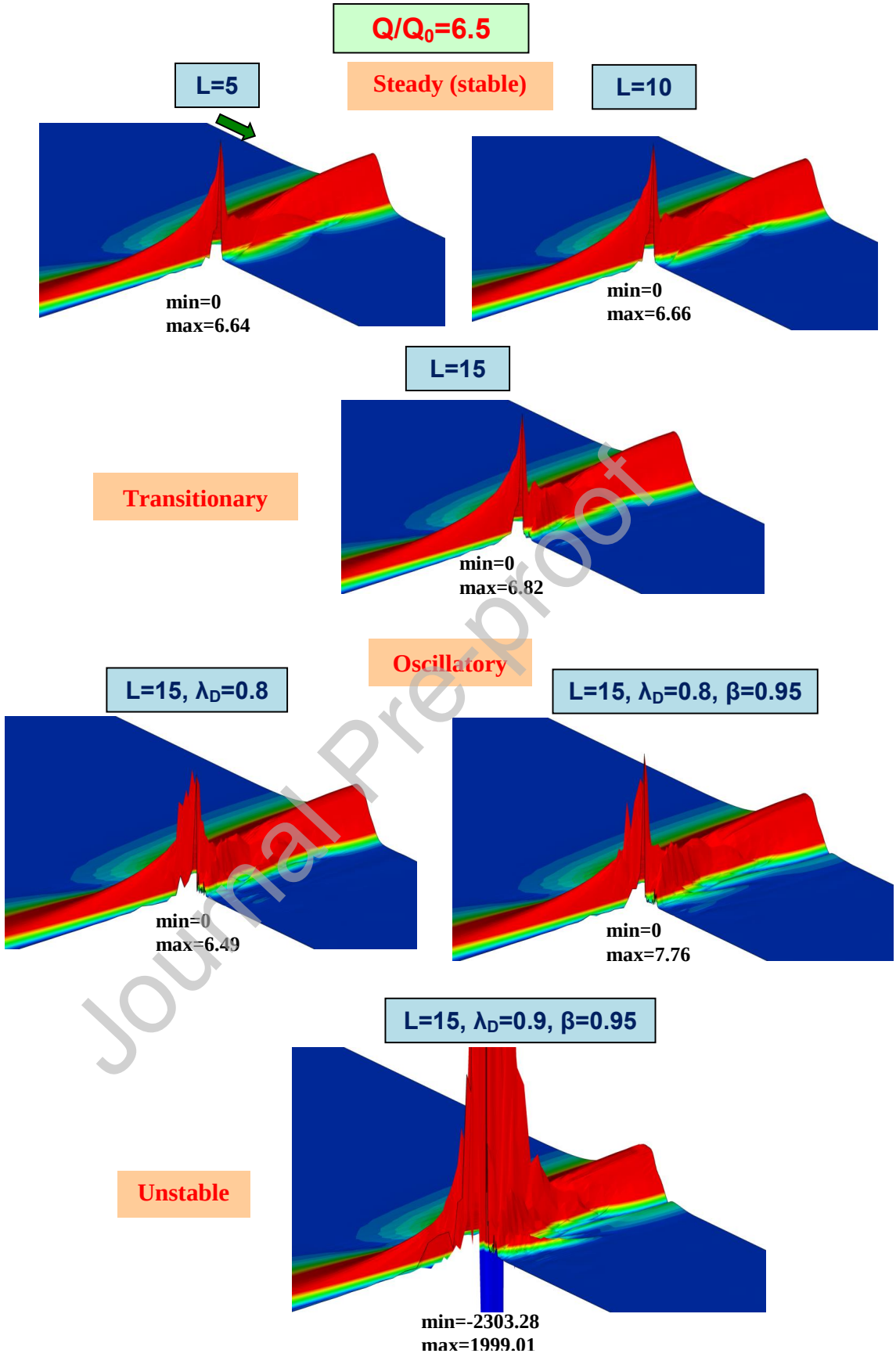

Fig. 13. Third invariant [$\Sigma_{gen}^{plane-abs} = -(0.5*\mathrm{I}_3)/(\delta_{reg}+\mathrm{I}_2)$ fields], *swIM* model; {(Q/Q_0), β, L, λ_D}={6.5,[0.9,0.95], [5-15], [0.6-0.9]}

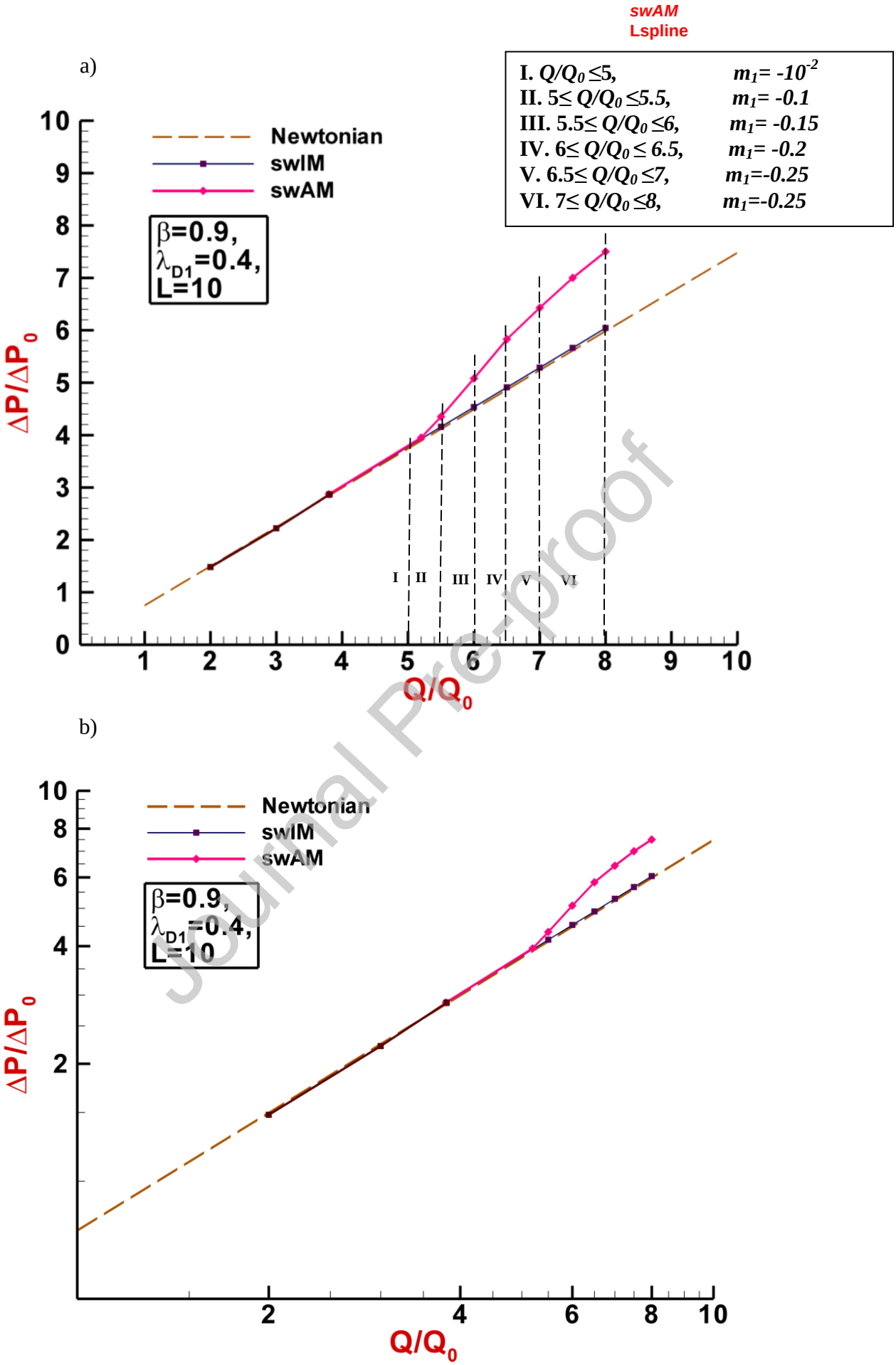

Fig. 14. Pressure-drop vs (Q/Q_0), *swIM* vs *swAM* model, a) linear scale, b) logarithmic scale

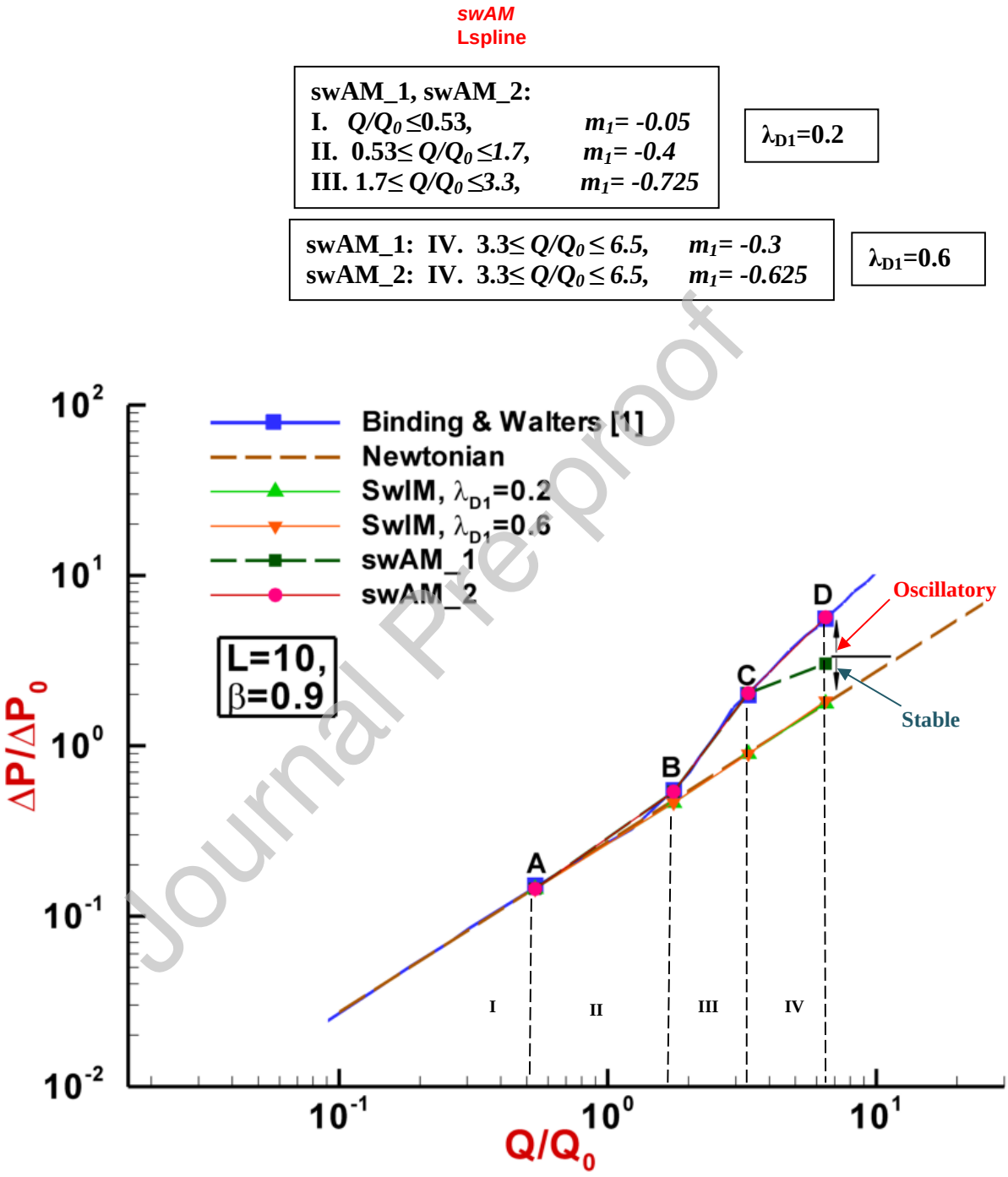

Fig. 15. Pressure-drop vs $(Q/Q_0)^{Exp}$, *swIM* vs *swAM* model, (logarithmic scale), The points A, B, C, D correspond to non-dimensional flow rates of 0.53, 1.7, 3.3 and 6.5, respectively in the planar geometry

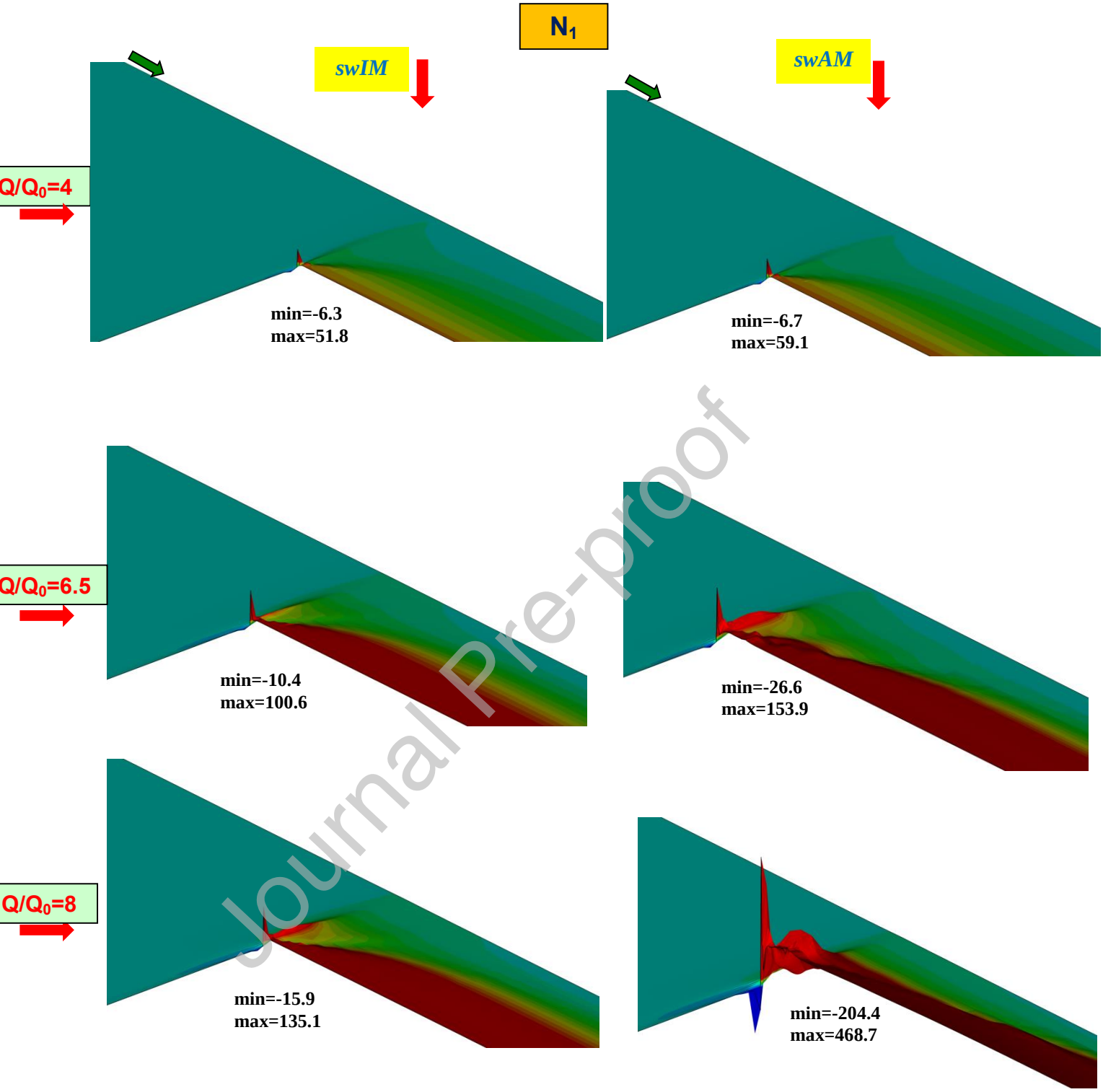

Fig. 16. First normal-stress difference ($N_1 = \tau_{11} - \tau_{22}$); *swIM* vs *swAM* ($m_1$=-0.25) model; {[$Q/Q_0$], β, L,λ_{D1}}={[6, 8.5, 10], 0.9, 10, 0.4}

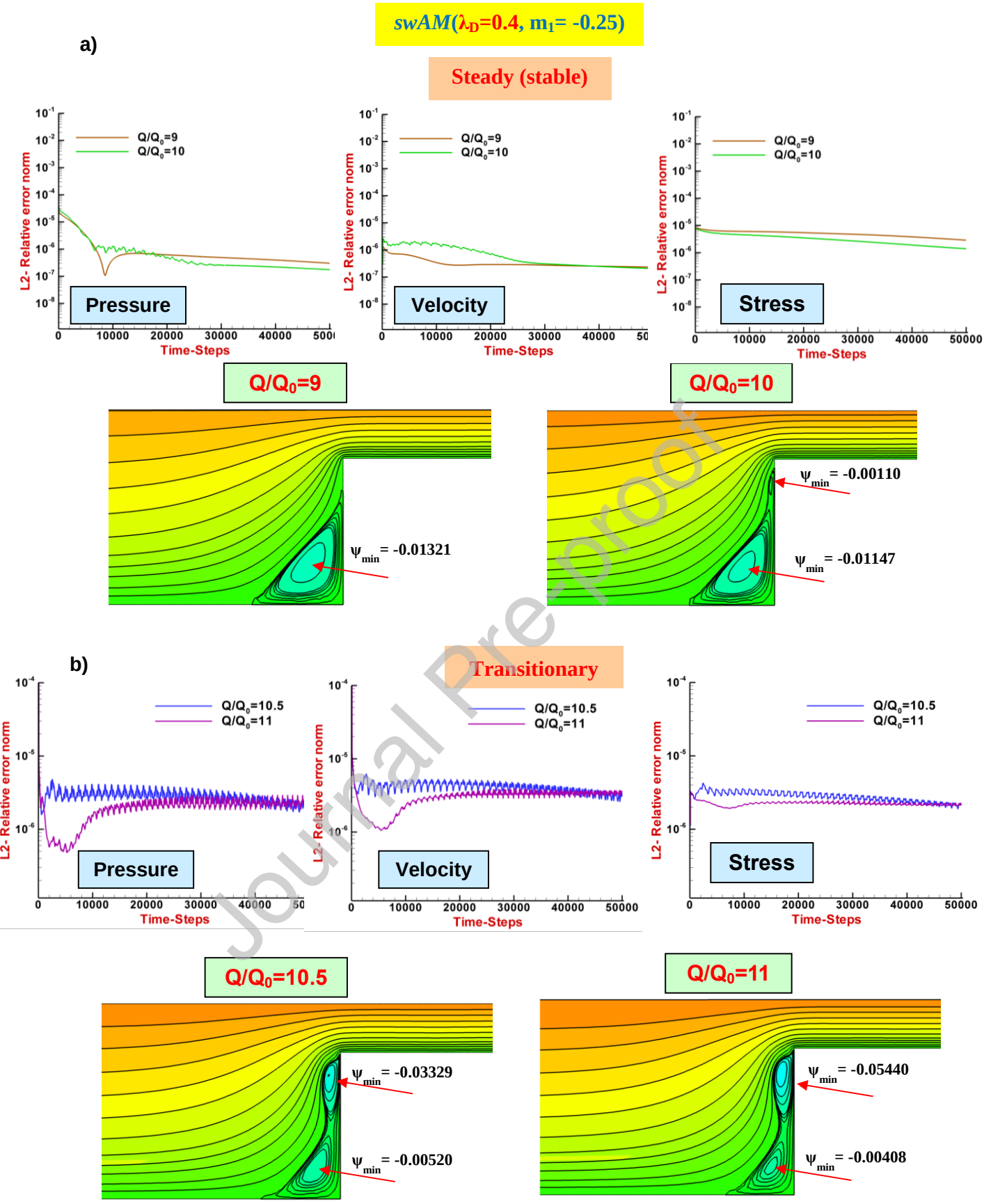

Fig. 17. Temporal convergence and streamlines, a) stable, b) transitionary, c) oscillatory/unstable, increasing Q, *swAM* model; $\{\beta, L, \lambda_{D1}, m_1\}=\{0.9, 10, 0.4, -0.25\}$

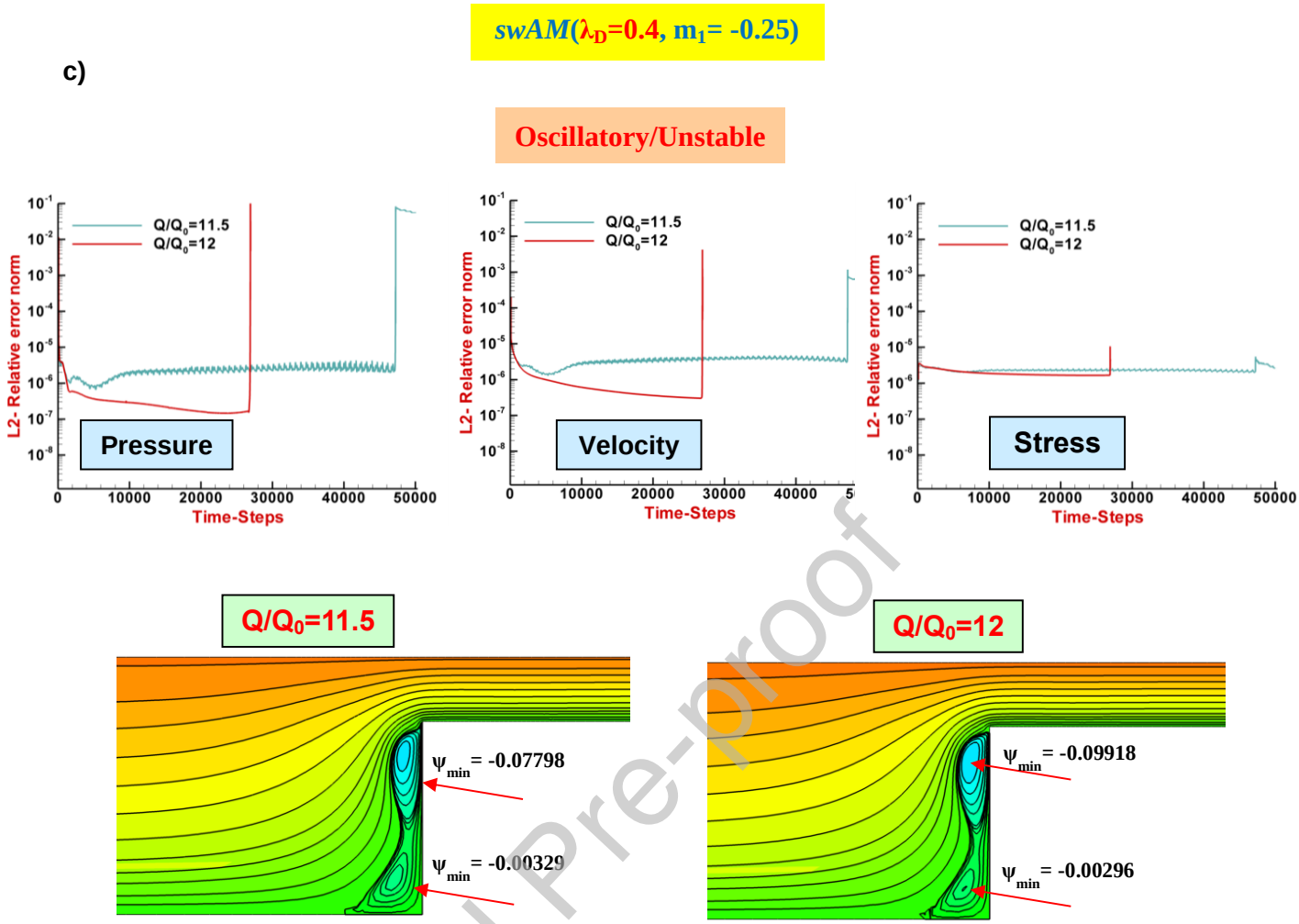

Fig. 17. Temporal convergence and streamlines, a) stable, b) transitionary, c) oscillatory/unstable, increasing Q, *swAM* model; $\{\beta, L, \lambda_{D1}, m_1\}=\{0.9, 10, 0.4, -0.25\}$

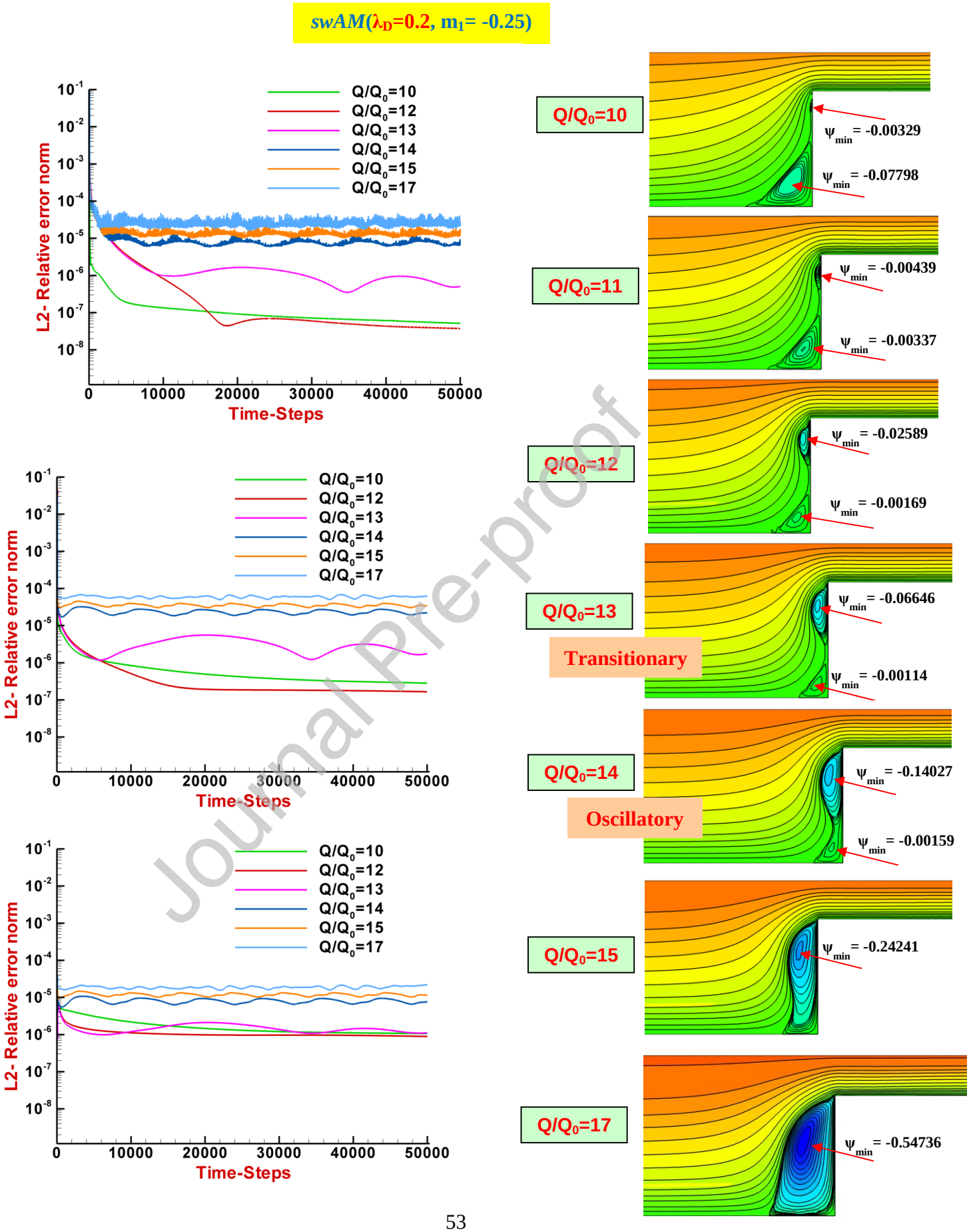

Fig. 18. Temporal convergence and streamlines, increasing Q, *swAM* model; $\{\beta, L, \lambda_{D1}, m_1\}=\{0.9, 10, 0.2, -0.25\}$

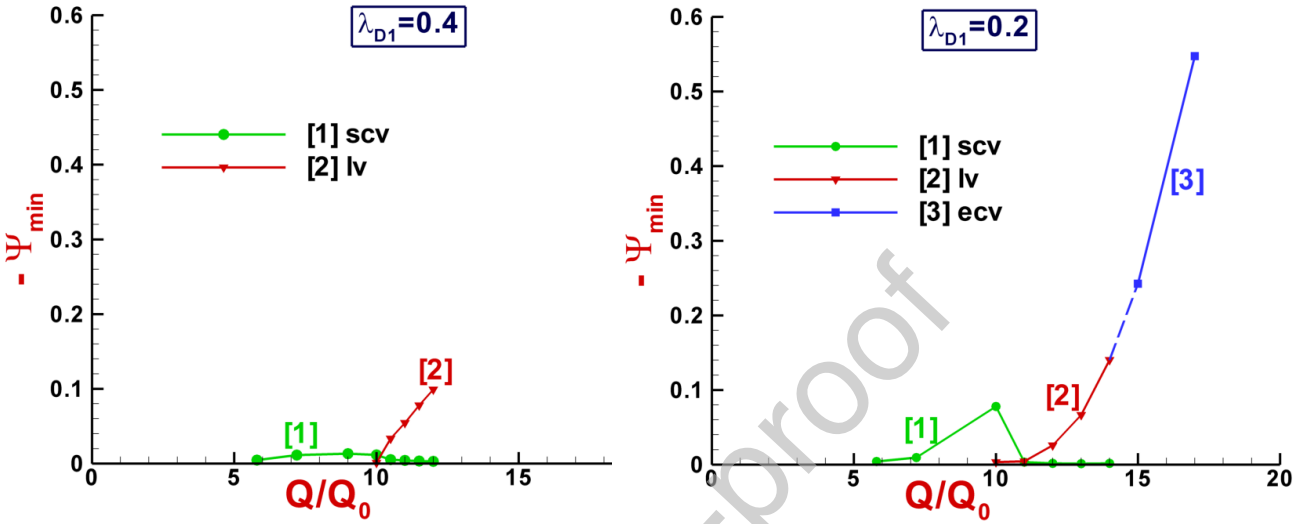

Fig. 19. Salient-corner (*svc*), lip-vortex(*lv*), and elastic-corner (*evc*) vortex intensity (ψ_{min}), *swAM*[L=10, λ_{D1}=(0.2, 0.4), β=0.9]